

5. SITE 1246¹

Shipboard Scientific Party²

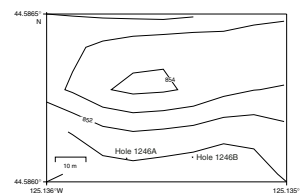
INTRODUCTION

Site 1246 (proposed Site HR1b) is located in 850 m of water ~3 km north of the southern Hydrate Ridge summit (see Fig. F1C, p. 51, in the “Leg 204 Summary” chapter). The three-dimensional (3-D) seismic data show that the bottom-simulating reflector (BSR) is at ~114 meters below seafloor (mbsf) at this site. This site also samples a pair of bright regional seismic reflectors, referred to as Horizons B and B’, at depths of ~60 and 100 mbsf, respectively. At this site, the temperature and pressure at the seafloor are well within the gas hydrate stability zone (GHSZ), indicating that gas hydrates can exist within the entire stratigraphic section above the BSR if hydrate-forming gases are available in concentrations that exceed their in situ solubility.

The primary objective at Site 1246 was to sample Horizons B and B’ where they are within the GHSZ. By comparing Site 1246 to Site 1244, where Horizons B and B’ are below the GHSZ, we hope to constrain lithologic and hydrologic explanations for the strong reflectivity of these seismic horizons, obtain insights into the processes that transport fluids into and through the GHSZ, and develop more effective strategies to predict the presence of hydrate from seismic and other remote-sensing data.

Two holes were drilled at Site 1246 (Fig. F1). Hole 1246A was drilled to a depth of 180 mbsf without coring to obtain the initial logging-while-drilling (LWD) data for this site. At Hole 1246B, we obtained 16 advanced piston corer (APC) cores, sampling to a depth of 136.7 mbsf with 99% recovery. Only basic sampling was conducted on these cores.

F1. Bathymetric map, p. 21.



¹Examples of how to reference the whole or part of this volume.
²Shipboard Scientific Party addresses.

OPERATIONS

Two holes were drilled at Site 1246 (Table T1), under good weather conditions. Wind speed was 5–25 kt, gusting to 28 kt; seas were 4–9 ft; swell was 6–12 ft; and the prevailing sea-surface current was from the north at ~0.5 kt. Hole 1245A was drilled for LWD on 19 July 2002, and we returned on 11 August, near the middle of Leg 204, to core Hole 1246B. The APC temperature (APCT) tool was run five times, and no other special tools were deployed at this site (see Table T4, p. 75, in the “Leg 204 Summary” chapter).

The first helicopter rendezvous took place at Site 1246 on Friday 19 July 2002. The helicopter arrived at 1247 hr and was away again with passengers at 1307 hr. Pressure core sampler (PCS) scientist Jerry Dickens and Fugro piezoprobe engineers Terry Langsdorf and Ko-min Tjok disembarked from the *JOIDES Resolution*, while sedimentologist Xin Su and HYACINTH engineer Thjunjoto came aboard.

Hole 1246A was spudded at 0300 hr on Friday 19 July, and we conducted LWD/measurement while drilling (MWD) from the seafloor at a drilling rate of 25–30 m/hr, to a depth of 180 mbsf without difficulty. Real-time data were transmitted to the surface to evaluate formation properties. Two stands were pulled up from total depth (TD) without rotating (sliding test) to evaluate the drilling effects on the Nuclear Magnetic Resonance (NMR-MRP) tool (see “Downhole Tools and Pressure Coring,” p. 14). Tools were pulled to the rig floor at 1900 hr, and the data from both Holes 1245A and 1246A were downloaded. Total bit run was ~20 hr.

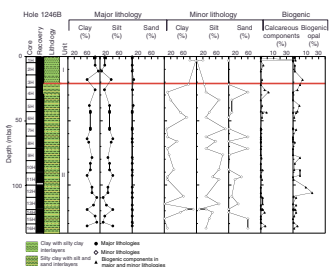
Hole 1246B was cored to 136.7 mbsf using the APC. Five measurements of in situ temperature were made using the APCT tool. No in situ pressure measurements were made, nor were any PCS cores taken at this site. There were no deployments of HYACINTH pressure cores.

LITHOSTRATIGRAPHY

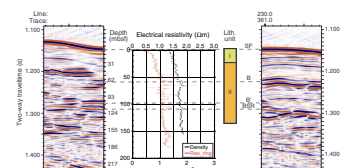
Site 1246 is located between Sites 1245 and 1244 just east of the crest of southern Hydrate Ridge (see Fig. F1, p. 51, in the “Leg 204 Summary” chapter). Seismic reflection profiles suggest that Horizon B and B', cored at Site 1244 below the BSR, are present at Site 1246 above the BSR (see Fig. F5, p. 55, in the “Leg 204 Summary” chapter). Two holes were drilled at Site 1246. One hole was logged with LWD (Hole 1246A), and one was cored (Hole 1246B) using the APC to 136.70 mbsf with 99% core recovery. Two lithostratigraphic units were defined at Site 1246 (Figs. F2, F3) based on sedimentological criteria (variations in sedimentary structure and grain size or biogenic and lithologic components) and correlation with other parameters. Lithostratigraphic Unit I is composed of dark greenish gray diatom-bearing clay. Lithostratigraphic Unit II contains dark greenish gray diatom-bearing clay with abundant silt and sand turbidites. We compare and correlate our results with the downhole LWD data (density and resistivity) and physical property measurement (magnetic susceptibility [MS]) to better define the entire stratigraphic sequence. We also discuss the 3-D seismic reflection data, which were used to correlate the stratigraphy at this site to that at Site 1244. Correlation of the lithostratigraphic units defined here with the other Leg 204 sites is summarized in Figure F10, p. 60, in the “Leg 204 Summary” chapter.

T1. Hole locations, p. 54.

F2. Lithostratigraphic summary, p. 22.



F3. East-west seismic reflection profile, p. 23.



Lithostratigraphic Units

Lithostratigraphic Unit I

Interval: Core 204-1246B-1H through Section 3H-5
Depth: Hole 1246B: 0.00–21.70 mbsf
Age: late Pleistocene–Holocene

Lithostratigraphic Unit I is mainly composed of dark greenish gray (5GY 4/1) clay with diatom-rich silty clay and nannofossil and diatom-bearing silty clay near the base of the unit (Fig. F2). Smear slides show >80% clay in samples above 15 mbsf in lithostratigraphic Unit I; as much as 20%–40% silt was observed in samples below 15 mbsf to the base of the unit. Biogenic components (mainly diatoms and calcareous nannofossils) in smear slides compose between 3% and 16% of the major and minor lithologies (Fig. F2). The abundance of siliceous components increases throughout lithostratigraphic Unit I, reaching 12% at 21.7 mbsf. Calcareous nannofossils are present in small amounts (2%–5%) and vary in abundance only slightly, except in a bioturbation burrow at 2.9 mbsf (Sample 204-1246B-1H-1, 140 cm), which contained up to 50% calcareous nannofossils (Fig. F2).

Bioturbation is more common in the upper 15 mbsf of lithostratigraphic Unit I, whereas sulfide patches or mottles increase in abundance toward the base of the unit; large patches (up to 3 cm² on the split-core surface) or irregular layers (up to 2 cm thick) of iron sulfide were observed in Sections 204-1246B-3H-3 to 3H-5.

Authigenic carbonates are present in Core 204-1246B-1H (e.g., at 2.65 and 3.65 mbsf) as light-colored crumbly patches. Smear slide observation suggests that these carbonates are dominantly composed of 90% calcite needles (Fig. F4).

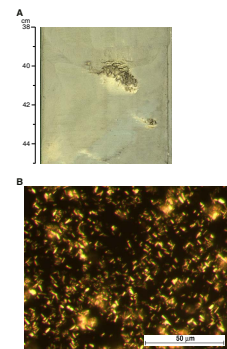
Lithostratigraphic Unit II

Interval: Sections 204-1246B-3H-5 through 16H-CC
Depth: 21.70–136.76 mbsf
Age: Pleistocene

Lithostratigraphic Unit II is composed of a series of fining-upward sequences of silt to silty clay. The sediment is dark greenish gray (5GY 4/1) to very dark gray (N3) where sulfides are present; the color varies to dark gray (N4) in 10- to 100-cm-thick intervals between 50 and 70 mbsf (Cores 204-1246B-7H through 8H). The top of lithostratigraphic Unit II is defined by the onset of graded silt and sand layers, interpreted as turbidites (at 21.7 mbsf) (Fig. F2). Lithostratigraphic Unit I lacks these sequences.

Grain size and mineralogy of both the major and minor components of lithostratigraphic Unit II were determined from smear slide analysis (Fig. F2). The dominant lithology is silty clay with variations in the amount of biogenic opal and few biogenic calcareous components. Silt to silty sand is the typical minor lithology observed in lithostratigraphic Unit II. These coarser layers commonly grade upward into silty clay from an erosional basal contact. The interval from 90 to 120 mbsf (Cores 204-1246B-11H through 13H) is slightly more clay rich than the rest of the lithostratigraphic unit, although silt and sand interlayers are still present throughout, as seen in the minor lithologies (Fig. F2). Prominent increases in the sand fraction (where >50% of the total sedi-

F4. Authigenic carbonate, p. 24.



mentary components is composed of sand) are observed at 62, 71, and 136 mbsf (Fig. F2).

Thin layers with high silt content (>60%) are present throughout lithostratigraphic Unit II and, in all cases, mark the base of a fining-upward sequence. Sections 204-1246B-7H-3 and 8H-3 contain two distinct >30-cm-thick silt horizons that correlate well with peaks in the MS data (see “**Magnetic Susceptibility**,” p. 12, in “Physical Properties”). Each MS peak associated with the silt layers has a width close to 2 m and is cut off at its upper boundary by another thinner silt layer. The sequences are bound by erosional contacts at both their upper and lower contacts. The thickness of each of these MS peaks is indicative of the total thickness of the fining-upward sequence. Interestingly, smear slide analyses show that these high-susceptibility intervals are quartz rich and do not contain an unusual abundance of iron-bearing minerals.

The biogenic components in lithostratigraphic Unit II were divided according to chemical composition. Calcareous biogenic components consistently compose <10% of the total sedimentary components in this unit (Fig. F2). Macroscopic foraminifers are found in Cores 204-1246B-6H, 7H, 8H, and 12H, but foraminifers only exceed 5% of the sedimentary components in Samples 204-1246B-6H-1, 74 cm, and 14H-2, 113 cm. Calcareous nannofossils do not exceed 4% of the sedimentary components in any sample from lithostratigraphic Unit II.

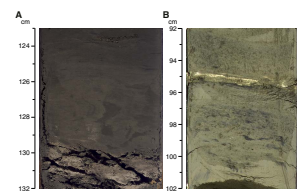
Siliceous biogenic components, unlike their calcareous counterparts, commonly compose >5% of the sediment and in Cores 204-1246B-9H, 10H, and 12H exceed 10% of the total sedimentary components. The overall siliceous microfossil content is slightly lower in the uppermost 50 m (from 21.7 to 71.7 mbsf) of lithostratigraphic Unit II (Fig. F2) than in the lower section of the unit. The sediments of seismic Horizon B (Fig. F3) (see “**Logging Units**,” p. 16, in “Downhole Logging”), which extends from 55.5 to 76 mbsf, are distinguished from those of the rest of lithostratigraphic Unit II by their lack of biogenic components. Horizon B is composed of quartz-rich dark gray silt and silty clay layers.

Seismic Horizon B', which is also sampled in lithostratigraphic Unit II (Fig. F3), is thought to be associated with a gas-charged interval of increased porosity caused by the presence of volcanic glass that is disseminated throughout Cores 204-1246B-10H and 11H. Two discrete volcanic glass-bearing layers (<1 and <0.1 cm thick, respectively) were found at 88 and 95 mbsf; the glass-bearing layer at 88 mbsf is directly above an interstitial water (IW) sample location and may be thicker than what was described in the core (Fig. F5). Samples 204-1246B-11H-2, 87 cm, and 11H-3, 43 cm, both contain >10% volcanic glass in their silt size fraction (Fig. F6).

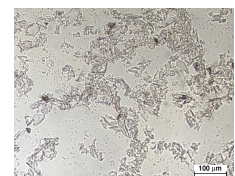
Sedimentary Evidence of Gas Hydrate

Five gas hydrate samples were taken from lithostratigraphic Unit II at 66.5, 96.6, 104.9, 105.1, and 109.5 mbsf (Samples 204-1246B-8H, 25–30 cm; 11H-5, 93–126 cm; 12H-4, 87–102 cm; 12H-4, 102–127 cm; and 13H-1, 0–30 cm). However, mousseliike textures were observed only in Sections 204-1246B-7H-1 and 14H-3, above and below the depths where hydrate was sampled. Additionally, the mousseliike texture that is present in Section 204-1246B-14H-3 is below the projected depth of the BSR at Site 1246 (see “**Introduction**,” p. 1) and is likely a product of coring-related disturbance rather than gas hydrate dissociation. Thermal anomalies indicative of the presence of gas hydrate correspond well to the bases of turbidites in Cores 204-1246B-7H and 8H (see “**Mag-**

F5. Volcanic glass horizon, p. 25.



F6. Volcanic glass shards, p. 26.



netic Susceptibility,” p. 12, in “Physical Properties”), although no textural evidence for the dissociation of gas hydrate was observed in these cores. If hydrate is disseminated in the pore space of the coarse-grained base of turbidites, soupy and mousselike textures typical of fine-grained sediment may not form and evidence for the presence of hydrate may be obscured.

Environment of Deposition

Correlation between Sites 1246 and 1244 is possible using Horizons B and B' (in lithostratigraphic Unit II) observed in the 3-D seismic data and the stratigraphic similarities observed in the cores from each site (e.g., Horizon B' contains volcanic glass at both sites and Horizon B is characterized by a thick turbidite couplet). Generally, lithostratigraphic Unit II, at both Sites 1244 and 1246, (1) is dominated by turbidites and (2) intersects the Horizon B and B' reflectors, which can be traced from site to site on the seismic data (see Fig. F5, p. 55, in the “Leg 204 Summary”). Horizons B and B' are offset by numerous normal faults, and the sediments at Site 1246 have been uplifted, and likely eroded, resulting in a much shallower position for Horizons B and B' at Site 1246. This evidence for uplift and erosion suggests that part or all of lithostratigraphic Unit I and perhaps the uppermost portion of lithostratigraphic Unit II from Site 1244 is likely not preserved at Site 1246.

Based on the above correlation, we infer that the turbidites observed in lithostratigraphic Unit II at Sites 1246 and 1244 were deposited in the same depositional environment and that subsequent uplift and erosion has since separated these once-continuous stratigraphies. Lithostratigraphic Unit I has less coarse-fraction sediment than lithostratigraphic Unit II at Site 1246. This suggests that sedimentation rates were higher during the deposition of lithostratigraphic Unit II than they were during the deposition of lithostratigraphic Unit I. Perhaps this change in sedimentation rate occurred in response to the uplift of Hydrate Ridge beneath Site 1246, which may have isolated the summit, allowing turbidites to pond only around its base and hemipelagic sediment to accumulate on its crest (as observed in the lithology of lithostratigraphic Unit I). Alternatively, erosion near the crest of a growing Hydrate Ridge may have removed a previously deposited stratigraphic sequence and only relatively recently replaced it with a younger drape of hemipelagic sediment. In either case, the fine-grained nature of lithostratigraphic Unit I compared to Unit II suggests a change in depositional environment. Whether this change represents a response to tectonic uplift or changes in the source region for the coarse material remains to be resolved.

BIOSTRATIGRAPHY

Site 1246 was drilled on the northern flank of the southern summit of Hydrate Ridge. Two holes were drilled, and one was cored. Hole 1246B, cored to 136.70 mbsf with 99% core recovery, recovered a Pleistocene–Holocene sedimentary sequence. Biostratigraphy for Site 1246 was based on examination of diatoms and calcareous nannofossils from all core catcher samples and from a few samples within cores from Hole 1246B.

Diatoms

Hole 1246B yields rare to common and poorly to moderately preserved diatoms. The interval from Samples 204-1246B-1H-CC through 3H-CC (4.69–23.95 mbsf) contains common diatoms, whereas diatoms are rare to few below this interval. The diatom assemblage in Hole 1246B is dominated by such species as *Stephanopyxis dimorpha*, *Stephanopyxis* spp., *Neodenticula seminae*, and *Thalassionema nitzschioides*.

The interval from Samples 204-1246B-1H-CC (4.69 mbsf) through 4H-CC (33.83 mbsf) contains *N. seminae* but does not contain *Proboscica curvirostris*. These samples were assigned to North Pacific Diatom Zone (NPD) 12 (*N. seminae* Zone). The last occurrence (LO) of *P. curvirostris* was placed between Samples 204-1246B-4H-CC (33.83 mbsf) and 5H-CC (43.22 mbsf).

Calcareous Nannofossils

The Pleistocene–Holocene sedimentary sequence in Hole 1246B generally yielded very few and poorly preserved calcareous nannofossils. However, samples from the middle part of the sequence in Hole 1246B (70.65–109.68 mbsf) contain rare to common and moderately to well-preserved calcareous nannofossils. Two late Pleistocene calcareous nannofossil events were determined based on the presence of bioevent marker species in these samples.

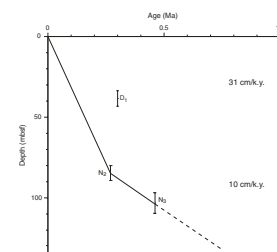
Emiliania huxleyi, in trace or rare abundance, was observed in a few core catcher samples of the top interval from 0 to 70.65 mbsf. Common and well-preserved, large-sized (~4 µm) *E. huxleyi* is present in Sample 204-1246B-9H-CC (80.22 mbsf). According to the study of Pujos-Lamy (1977a, 1977b), such large-sized forms of *E. huxleyi* are present in the early evolutionary stage of this species. The top interval (0–80.22 mbsf) was assigned to Zone NN21. Sample 204-1246B-10H-CC contains abundant *Gephyrocapsa* spp. but lacks *E. huxleyi* and *Pseudoemiliania lacunosa* and was assigned to Zone NN20. The LO of *P. lacunosa* observed in Sample 204-1246B-12H-CC (109.68 mbsf) marks the NN19b/NN20 zonal boundary. Rare to common, but not abundant, small *Gephyrocapsa* spp. are present in the bottom sequence of Hole 1246B from 122.57 to 136.71 mbsf, suggesting an age of younger than 1.0 Ma for the interval.

Summary

Based on an analysis of diatoms and calcareous nannofossils from the Pleistocene–Holocene sedimentary sequence in Hole 1246B, three microfossil events (i.e., one diatom and two nannofossil events) were recognized (Table T2). The LO of *P. curvirostris* (0.3 Ma) was found 40–50 m above the first occurrence (FO) of *E. huxleyi* (0.27 Ma) (Fig. F7), indicating a discrepancy between these two events in this hole. A very few *P. lacunosa* (LO at 0.46 Ma) found in the interval from 43.22 to 61.66 mbsf were considered to be reworked fossils. Similarly, the presence of *P. curvirostris* above 80.22 mbsf could also be caused by reworking. However, the presence of *P. curvirostris* is continuous in the interval from 43.22 mbsf to the bottom of the hole, and no indication of reworking was found in the diatom assemblage. Detailed postcruise studies on these two microfossil groups are needed to understand the discrepancy. In this report, we did not use the LO of *P. curvirostris* for estimating sedimentation rates because of the possibility of reworking. The age of the

T2. Bioevents, p. 55.

F7. Age-depth plots, p. 27.



sequence at the bottom of Hole 1246B is suggested to be younger than 1.0 Ma based on the diatom and calcareous nannofossil assemblages.

We estimated the linear sedimentation rates using only two nannofossil events, as discussed above. The sedimentation rates are 31 cm/k.y. for the interval from the top of Hole 1246B to 85 mbsf and 10 cm/k.y. for the interval from 85 to 105 mbsf.

INTERSTITIAL WATER GEOCHEMISTRY

The main objectives of the IW program at this site were to provide geochemical proxies for the presence and abundance of gas hydrate and to establish constraints on the nature of the seismic reflectors, B and B', observed in the seismic data. At Site 1246, these reflectors are present at ~60 and ~100 mbsf, which are above the depth of the BSR. In contrast, at Site 1244, these seismic reflectors are present below the BSR (see **“Introduction,”** p. 1). Only one hole was cored at Site 1246, and we recovered 33 IW samples at a frequency of approximately two whole rounds per core. The IW geochemistry data are tabulated in Table T3 and are illustrated in Figure F8.

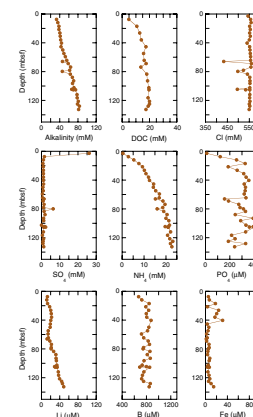
Site 1246 was cored to a total depth of 132 mbsf (Hole 1248B) just below the BSR, which in the seismic data lies at 114 mbsf (see **“Introduction,”** p. 1). Thus, the bulk of the IW data obtained at this site lies within the GHSZ. The composition of pore water in this zone is influenced by gas hydrate geochemistry and by the possible effect of the presence of Horizon B above the BSR.

Chloride Concentration and the Presence of Gas Hydrate

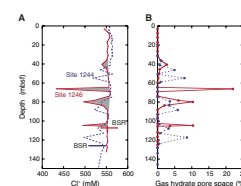
The downhole chloride content exhibits similar overall features to those previously observed in pore water recovered from Sites 1244 and 1245 in that the excursions to low chloride values are present in a well-defined zone ranging from the FO of gas hydrate at ~40 mbsf to the inferred depth of the BSR at ~114 mbsf. These chloride anomalies reflect dissociation of gas hydrate during recovery and can be used to estimate the amount of gas hydrate present in the sediments when used in conjunction with background in situ chloride data (see **“Interstitial Water Geochemistry,”** p. 13, in the “Explanatory Notes” chapter and **“Interstitial Water Geochemistry,”** p. 13, in the “Site 1244” chapter). We assumed anomalous low chloride values relative to the background concentration defined by data points that appear to fit a smooth profile at this site, as indicated by the shaded portion of the chloride distribution shown in Figure F9A. These background values correspond fairly well to the chloride concentrations obtained for Site 888, located west of the deformation front, which showed no evidence for the presence of gas hydrate (Kastner et al., 1995). At Site 1246, gas hydrate was indeed recovered from sediments where low chloride anomalies were observed (see **“Lithostratigraphy,”** p. 2). In addition, thermal anomalies seen in infrared (IR) data (see **“Physical Properties,”** p. 10) and variations in LWD resistivity data (see **“Downhole Tools and Pressure Coring,”** p. 14) also suggest the presence of gas hydrate from ~40 mbsf to the BSR. Estimates on amount of gas hydrate based on the Cl⁻ anomalies range from 0% to a single-point maximum of 20% of the pore space.

T3. Dissolved species in pore waters, p. 56.

F8. Concentration profiles of dissolved species in pore water, p. 28.



F9. Chloride concentration profile, p. 30.



Sulfate, Methane, and the Sulfate/Methane Interface

As a result of the IW sampling frequency of only two whole rounds per core, the shape of the sulfate profile cannot be constrained, nor can an estimate of methane flux be given for Site 1246. Headspace methane concentrations (Table T4) (also see “Organic Geochemistry,” p. 8) locate the sulfate/methane interface (SMI) at ~7 mbsf.

Major and Minor Element Distributions

Lithium is a highly mobile alkali ion, and its chemical mobility is strongly dependent on temperature (Edmond et al., 1979; Seyfried et al., 1984). At Site 1246, a release of lithium from aluminosilicates at depths below 1 km, where the formation temperature exceeds 80°C, is documented by an overall increase in its concentration with depth. Superimposed on this trend we observe a minimum in the lithium concentration at the depth of seismic Horizon B (Fig. F10), which reflects incorporation of this element into clay minerals during alteration of volcanic material at low temperatures. At both Sites 1244 and 1246, the depth of the interval associated with Horizon B corresponds to a decrease in the dissolved lithium concentration, as shown in Figure F10.

The distribution of dissolved iron at Site 1246 shows a pattern similar to that observed at Site 1244, with an increase to a maximum of 30 μM at 40 mbsf (Fig. F11). This distribution likely reflects cycling of iron minerals, which are precipitated as iron sulfides below the SMI and are remobilized at depth. The dissolved iron remains higher than the background levels (<3 μM) throughout the GHSZ. Postcruise analyses of the distribution and isotopic composition of dissolved sulfide and of sulfide minerals will likely provide constraints on the nature of the iron biogeochemical cycling at this site.

ORGANIC GEOCHEMISTRY

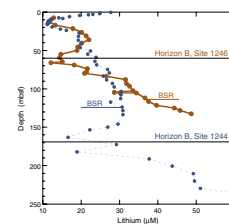
Site 1246 is located on the eastern flank of Hydrate Ridge and was cored to sample the Horizon B/B' reflector pair in a position above the BSR. These reflectors were originally thought to be carbonate layers along permeable horizons. The shipboard organic geochemistry program at Site 1246 included analyses of hydrocarbon gases, carbonate and organic carbon (OC), total sulfur (TS), and total nitrogen (TN) content. A description of the methods used for these analyses is summarized under “Organic Geochemistry,” p. 16, in the “Explanatory Notes” chapter.

Hydrocarbon Gases

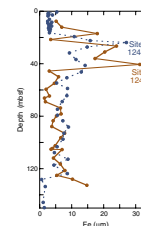
The levels of methane (C₁), ethane (C₂), ethylene (C₂₌), and propane (C₃) remaining in cores were measured using the headspace technique. The results are reported in Table T4 and plotted as parts per million by volume (ppmv) of gas component vs. depth in Figure F12. Methane content increases rapidly from levels of 3 to 18 ppmv in the shallowest samples at 0–3 mbsf, to ~4,900 ppmv at a depth of 7.7 mbsf, and to levels of 10,000–60,000 ppmv at greater depths. This sharp increase in headspace methane occurs at the approximate depth of the SMI, as seen at Sites 1244, 1251, and elsewhere. The vial headspace ppmv C₁ concentration was recalculated to express the millimolar methane concentra-

T4. C₁, C₂, C₃, p. 57.

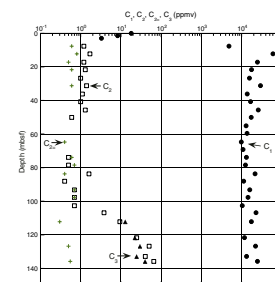
F10. Lithium concentration, p. 31.



F11. Profiles of iron, p. 32.



F12. Headspace gas concentrations of C₁, C₂, C₂₌, and C₃ vs. depth, p. 33.



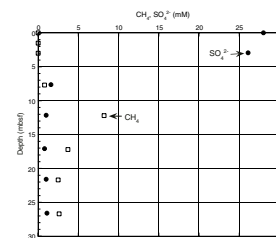
tions remaining in the cores (see “Organic Geochemistry,” p. 16, in the “Explanatory Notes” chapter). These estimates of absolute gas concentration are meaningful only in shallow zones where sediments are undersaturated or slightly supersaturated with respect to dissolved methane at surface conditions. The calculated dissolved CH_4 concentration is shown in Figure F13, along with the sulfate depletion profile (see “Sulfate, Methane, and the Sulfate/Methane Interface,” p. 8, in “Interstitial Water Geochemistry”). Although the sample spacing at Site 1246 is not optimal for purposes of defining the depth of the SMI, the general pattern is consistent with this horizon being at a depth of ~8 mbsf.

C_2 content is maintained at low levels (1–2 ppmv or below detection) in headspace analyses of cores from Site 1246 in the depth interval from the seafloor to ~105 mbsf. $\text{C}_{2=}$ is present at trace levels (0.3–2 ppmv) throughout the depth interval cored, whereas C_3 traces are present in headspace gas only for samples below depths of 112 mbsf (Table T4; Fig. F12).

The composition of gas samples from voids or expansion gaps in the core liner are listed in Table T5 and plotted in Figure F14. The void gas (“vacutainer”) samples are relatively pure methane, generally with minimal air contamination. The methane content in the core voids from Hole 1246B is generally >925,000 ppmv (>92.5% by volume). The ethane content of void gas shows a more stepwise increase pattern with depth at Site 1246. Ethane increases from 9 to 37 ppmv in the interval from 35 to 102.2 mbsf. In the next sample at 110.2 mbsf and deeper, the ethane content increases abruptly to a range of 350–640 ppmv. This increase in the relative ethane content is also apparent in the headspace gas analyses over the depth interval from 102.7 to 107.2 mbsf. Propane is generally absent from void gases within the depth interval where gas hydrates are stable. One sample at 24.7 mbsf has 7 ppmv of propane, but this sample is probably above the depth where gas hydrate is present (Table T5; Fig. F14). The absence of propane in void gas samples over the depth interval 36–110 mbsf is consistent with the gas being derived from decomposition of Structure I methane hydrate, which can contain ethane but excludes propane. Although the increase in ethane content beneath the GHSZ could be partly a result of the release of ethane from decomposed gas hydrate, the increase in propane and isobutane is more likely the result of migrated hydrocarbons.

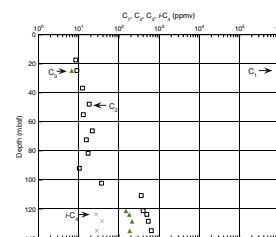
Gas composition expressed as C_1/C_2 of headspace and void gas is plotted vs. depth in Figure F15. The C_1/C_2 ratios for both headspace and void gas do not show any systematic decrease other than the marked offset discussed above, which is a result of an increase in ethane content in sediments beneath the gas hydrate occurrence zone. This change in the gas composition occurs at a core depth of ~105 mbsf and correlates with the deepest chloride anomaly (104.87 mbsf) at Site 1246 (see “Chloride Concentration and the Presence of Gas Hydrate,” p. 7, in “Interstitial Water Geochemistry”). The base of the GHSZ, as inferred from gas and pore water composition, is shallower than the depth of the BSR calculated from seismic data (114 mbsf). The discrepancy is even greater for depth of the base GHSZ (149 mbsf) estimated from the measured temperature gradient (0.049°C/m) and the methane-seawater pressure-temperature equilibrium.

F13. Dissolved residual methane and sulfate in pore water, p. 34.

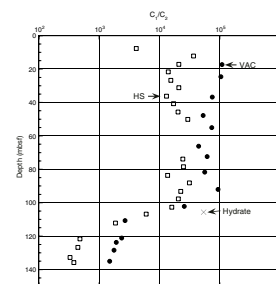


T5. Concentrations of light hydrocarbon and nonhydrocarbon gases from core gas voids, p. 58.

F14. Concentrations of C_1 , C_2 , C_3 , and $i\text{-C}_4$ vs. depth, p. 35.



F15. C_1/C_2 ratio vs. depth, p. 36.



Gas Hydrate

A single gas hydrate sample from Section 204-1246C-12H-4 (at 105 mbsf) was analyzed for hydrocarbon composition, with the results given in Table T6. The gas from the analyzed sample was ~92% methane, with 5% air contamination. Interestingly, the gas from this hydrate sample contained 8.3 ppmv of propane, a component that should be excluded from Structure I hydrate, along with 17.1 ppmv of ethane. It is not known if this trace of propane was actually present in the gas hydrate or if it was present in some of the sediment associated with the gas hydrate. The C_1/C_2 ratio of the gas from the gas hydrate is about the same as in void gas samples from this depth at Site 1246 (Fig. F15).

Carbon Analyses, Elemental Analyses, and Rock-Eval Characterization

A total of 16 sediment samples (one per core) were analyzed for carbonate carbon (IC), total carbon (TC), OC (by difference), TN, and TS. The results are listed in Table T7. Carbonate carbon content (Fig. F16) varies from 0.14 to 0.81 wt% at Site 1246. When calculated as $CaCO_3$, the carbonate contents measured in the Hole 1246B sediments vary from 1.14 to 6.75 wt% (Fig. F16). The analyzed samples near the proposed depths of the Horizon B/B' reflectors do not appear to be enriched in calcium carbonate.

OC content varies from 0.37 to 1.68 wt% (average = 1.20 wt%) (Table T7; Fig. F16). The highest OC content measured is 1.68 wt% at a depth of 185.95 mbsf. Although nitrogen contents are low (0.06–0.20 wt%), the C/N ratio is generally <10, which is consistent with a dominantly marine source of organic matter. Sediment samples have TS contents ranging from 0.11 to 1.25 wt% (Table T7), with no distinct relation to OC content.

The results of Rock-Eval pyrolysis of selected samples are given in Table T8. This analysis was performed in part to evaluate the possible presence of migrated liquid hydrocarbons. Although the production index values seem moderately elevated (i.e., >0.1), they are fairly typical for continental margin sediments cored by the Ocean Drilling Program (ODP). There is no correlation between increased C_{2+} gas components and higher production index values, and no definitive evidence for oil staining.

PHYSICAL PROPERTIES

At Site 1246, we used Hole 1246B for physical property analyses. This site is close to the previously cored Site 1244 and allows a lateral comparison of their lithologic characteristics, especially regarding Horizon B.

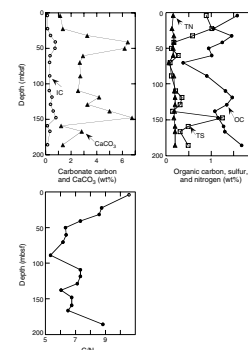
Track-mounted IR imaging of the core liner on the catwalk was used to determine the thermal state of the cored sections, whereas the handheld IR camera was used for rapid detection of cold anomalies. Four hydrate samples were selected based on IR images and subsequently sampled at this site.

Standard measurements for physical properties were carried out (see “Physical Properties,” p. 22, in the “Explanatory Notes” chapter). In addition, the automated shear vane and the three different velocity probes mounted on the Hamilton Frame were used in the upper two

T6. Light hydrocarbons and non-hydrocarbons from gas hydrate, p. 59.

T7. Contents of IC, OC, TN, and TS, and C/N ratios, p. 60.

F16. Downcore variation in IC, OC, TN, TS, and C/N ratios, p. 37.



T8. Rock-Eval pyrolysis of samples, p. 61.

cores to determine shear strength and velocity anisotropy (PWS1, PWS2, and PWS3), respectively.

Infrared Scanner

IR imaging of the cores drilled in Hole 1246B provided identification of hydrate zones in each core on the catwalk, as described in “[Infrared Scanner](#),” p. 25, in “Physical Properties” in the “Site 1244” chapter and in “[Infrared Thermal Imaging](#),” p. 23, in “Physical Properties” in the “Explanatory Notes” chapter. This information was used to facilitate hydrate sampling and preservation for all cores. The IR thermal anomalies are cataloged in Table T9, including an interpretation of the overall hydrate texture for each anomaly. The majority of the hydrate detectable by IR imaging at this site (76%) is present as disseminated layers. Veins, parallel to or crosscutting bedding, account for 16% of IR-detected hydrate. In contrast to Hole 1248B, nodular textures account for only 8% of hydrate detected by IR.

Successive thermal images were used to produce a downcore thermal log for each core recovered in Hole 1246B (Fig. F17). The logs show the overall thermal structure of each core. Strong cold anomalies are present from 66 to 109 mbsf, which correspond to the locations of hydrate samples. The temperature anomalies created by the hydrate were extracted by examination of the downcore temperature data and by direct examination of IR images. Figure F18 shows the magnitude of the temperature anomalies as function of depth. Subtle cold anomalies are first present at 16 mbsf, and distinct anomalies start at ~33 mbsf. The magnitude of ΔT increases toward the BSR, and minor cold anomalies extend below the BSR by ~3 m. Below 117 mbsf, temperature anomalies are probably a result of causes other than hydrates (e.g., contact with cold drilling fluid during extended core barrel coring or gas expansion or exsolution). The IR thermal anomalies that are attributed to hydrates are consistent with pore water saturation (S_w) from LWD (see Fig. F18), except from 15 to 45 and 106 to 118 mbsf, where the current interpretation of LWD logging results shows no hydrate, whereas IR results suggest the presence of relatively small amounts of hydrate.

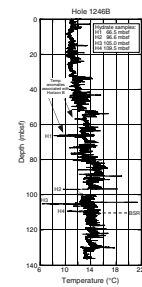
The extent of cold thermal anomalies to a depth of 117 mbsf, which is 3 m below the BSR depth of 114 mbsf is probably within the combined uncertainty of the estimated BSR depth and the curated core depth.

The preponderance of both disseminated and stratigraphically conformable veins of hydrate in Hole 1246B suggests that differences in permeability and porosity related to bedding may control the presence of hydrate at Site 1246. Stratigraphic control of the presence of hydrate in the overall context of Site 1246 is discussed below.

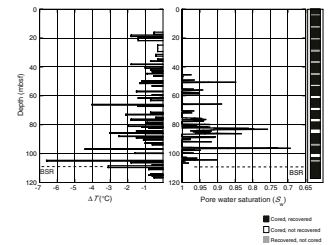
The presence of concentrated hydrate is often associated with intensive gas expansion cracks and voids, as illustrated in Figure F19 for Section 204-1246B-8H-4. These voids and cracks have a much higher IR temperature than the surrounding hydrate-bearing sediment. Thus, the overall cold-spot anomaly is often broken up into small intervals interrupted by the relatively higher temperature voids. By removing the voids and artificially compressing the hydrate-bearing intervals, gas hydrate in Section 204-1246B-8H-4 would yield a cold-spot thermal anomaly with a total length of 55 cm.

T9. IR anomalies, p. 62.

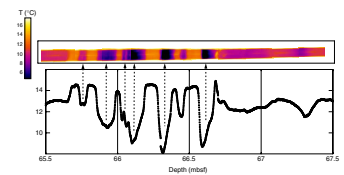
F17. Downcore temperature, p. 38.



F18. Comparison of IR anomalies and S_w , p. 39.



F19. Hydrate anomaly, p. 40.



Sediment Density from Multisensor Track and Moisture and Density

Sediment density values were measured with the multisensor track (MST) gamma ray attenuation (GRA) sensor (GRA density) and were also derived from discrete moisture and density (MAD) samples (bulk density) (Table T10). Both curves are in very good agreement and correlate to the LWD density values (Fig. F20), except that the correlated LWD data are slightly deeper by ~2–3 m. Sediment density values generally increase with depth from around 1.6 g/cm³ at the seafloor to ~1.8 g/cm³ at 140 mbsf. Two distinct zones of increased densities are identified at 55 and 65 mbsf. These zones correspond to intervals of high MS (see below). MAD indicate that these zones are also characterized by very low porosity values at ~45%–50% compared to the intervals above and below, which show porosities in the range of 55%–65%. The grain density does not show much variation with depth, with most of the values falling in the range between 2.6 and 2.8 g/cm³.

Magnetic Susceptibility

The most prominent features in the MS record are the two strong events at 55 and 65 mbsf (Fig. F20). These two MS anomalies can be correlated to the seismic Horizon B (Fig. F21). Close inspection of the sedimentological record indicates that the MS anomalies correlate to large turbidite events. Those turbidite sequences are dominated by quartz-rich layers (see “Lithostratigraphic Unit II,” p. 3, in “Lithostratigraphic Units” in “Lithostratigraphy”). The MS signals of both events are sharply truncated at the top and bottom, and they extend over a depth range of ~2.5 m each (Fig. F22). MAD data in this interval indicate an increase in density of ~0.2 g/cm³ and a decrease in porosity of ~15%. Grain densities remain near constant across this interval, however. The turbidite records are also closely related to the presence of hydrate.

Close inspection of the IR images showed that the base of each of the MS anomalies associated with Horizon B correspond to a cold-spot anomaly, which is an indication of the presence of hydrate (Fig. F22). The base of the MS anomaly is an interval where the more coarse-grained material is deposited. This is in general agreement with the hypothesis that gas hydrates form preferably in coarser-grained material (e.g., Lee and Dillon, 2001; Dallimore et al., 1999).

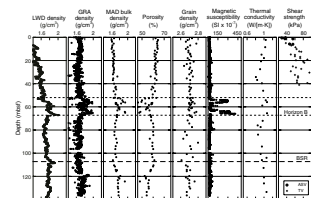
There is a slight mismatch in aligning the sedimentological record with the measurements on the MST and the IR images. It should be noted that the IR images were taken on the catwalk before the sediment cores were curated. A typical procedure after IR imaging is to close gas-expansion voids by compressing the sediments in the liner with a handheld piston. This results in fewer but larger voids, which fall at section boundaries. When core sections are split, the relative position of voids can shift, causing offsets between MST and the visual core descriptions. This explains the mismatch between MST measurements made on the whole-round core and the sedimentological record determined on the archive half of the split cores.

Non Contact Resistivity System

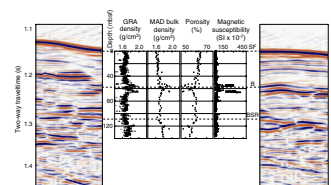
The Non Contact Resistivity (NCR) system is very sensitive to cracks and voids induced by gas expansion of the cores. The voids act like in-

T10. Moisture and density, p. 63.

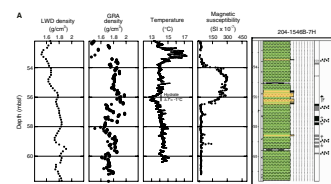
F20. Physical property data, p. 41.



F21. 3-D seismic and physical properties, p. 42.



F22. Sedimentology and physical properties, p. 43.



sulators and result in high resistivity values dominating the downcore trend (Fig. F23). The lower limit of the resistivity values can be used to estimate sediment resistivity; however, data values scatter significantly as a result of the effects of gas expansion. Within the upper 10 mbsf, where the gas expansion is less dominant, good correlation between the noncontact resistivity (NCR), compressional (P -) wave velocity (V_p), and gamma density is observed (Fig. F24).

Compressional Wave Velocity from the Multisensor Track and Hamilton Frame

A detailed investigation of V_p was carried out in Cores 204-1246B-1H and 2H, which did not suffer from strong gas-expansion cracks (Table T11; Fig. F24). Velocities were measured using the MST on the whole-round cores and also using the three different velocity sensors of the Hamilton Frame on the split cores. Measurements were only reliable to a depth of ~4.5 mbsf for the MST, but we were able to measure velocities to a depth of 10 mbsf from the split-core sections. Note that the reported velocity values are uncorrected for in situ temperature. Cores were measured after a temperature equilibration time of >4 hr.

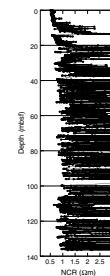
In general, V_p measured from the MST are slightly lower than those measured on the split cores. On average, the difference is ~30–40 m/s. This could be due to either the effect of a systematic shift of the Hamilton Frame sensors (inaccurate calibration) or drying of the split core over time. It was noted that the cores lost considerable amounts of moisture during storage on the core racks before splitting. The loss of water may explain the slightly higher velocity values measured on the split cores. The MST velocity record shows some high-resolution variability with intervals of increased values at ~1 and 3.5 mbsf. These intervals correspond to zones of higher density as seen in the GRA record (Fig. F24) and slightly higher resistivity (Fig. F24).

The three V_p sensors on the Hamilton Frame measure the velocity of split cores in the x-, y-, and z-directions, respectively, and these measurements can be used to analyze the presence of any velocity anisotropy. It was observed that the PWS1 velocity (z-direction) (i.e., sound waves travel perpendicular to the bedding plane) was consistently slower than the other two velocities. Velocities in the x-direction were always higher by ~20 m/s. This can be an effect of velocity anisotropy caused by bedding. Within the upper 10 m, bedding is almost parallel to the seafloor. Therefore, the velocity measured across the sedimentation direction (z-component) is lower than that along the bedding (x-direction). The velocity along the y-direction was observed to be close to that in the x-direction, which is an expected trend; the two values begin to differ at depths below 6 mbsf. This could be the effect of developing gas-expansion cracks, which can also be seen in the NCR record, as the resistivity values begin to show significant scattering (Fig. F24B).

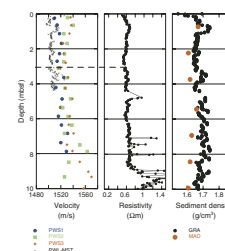
Thermal Conductivity

Thermal conductivity was routinely measured on the temperature-equilibrated whole-round core sections. Measured values vary between 0.81 and 1.07 W/(m·K) with a mean of 0.965 W/(m·K) (Fig. F20; Table T12). Thermal conductivity decreases from the seafloor to ~35 mbsf and is slightly higher in the interval from 40 to 80 mbsf. Below 80 mbsf, thermal conductivity increases almost linearly with depth.

F23. Downhole measurements of resistivity, p. 45.



F24. Comparison of V_p with NCR and bulk density, p. 46.



T11. V_p data, p. 64.

T12. Thermal conductivity, p. 65.

Shear Strength

Shear strength was measured in cores from within the upper 40 mbsf of Hole 1246B (Table T13; Fig. F20). We used the handheld Torvane as well as the automated shear vane. The two different systems are generally in very good agreement. Shear strength increases with depth from values of ~30 kPa at shallow depth to ~80 kPa at 40 mbsf. Extensive gas expansion of the cores resulted in inaccurate values (3.0–5.8 kPa) at greater depth.

Summary and Discussion

Physical properties measured at Site 1246 match well with the major lithostratigraphic units, especially Horizon B. Horizon B can be traced over a length of several kilometers on 3-D seismic profiles and was cored at Sites 1246 and 1244 (see Fig. F5, p. 55, in the “Leg 204 Summary” chapter). It is mainly characterized by the presence of large turbidite events that are associated with high MS values. Sediment density increases within these sequences with values ~ 0.2 g/cm³ larger than the over- and underlying sediments. The horizon consists of a minimum of two large turbidite events, each ~2.5 m thick, with a clear fining-upward sequence. The bottom of each sequence is associated with the presence of gas hydrate.

DOWNHOLE TOOLS AND PRESSURE CORING

Downhole Temperature Measurements

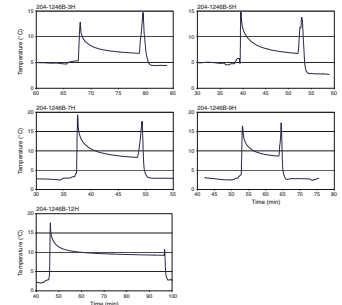
Five measurements of in situ temperature were made in Hole 1246B using the APCT tool (Table T14; Fig. F25). Data were modeled using the software program TFIT (as described in the “Downhole Tools and Pressure Coring,” p. 34, in the “Explanatory Notes” chapter), using measured thermal conductivities (see “In Situ Temperature Data Reduction,” p. 36, in “Physical Properties” in the “Explanatory Notes”). Uncertainty in the extrapolated value of in situ temperature, as a result of subjective analyst picking of t_p , t_i and t_r , is <0.02°C for these high-quality records. Uncertainty because of possible errors in measured values of thermal conductivity is also estimated to be ~0.02°C.

The resulting temperature estimates are shown in Figure F26. They show considerable scatter. Based on a decrease of ~2.2% in the apparent bottom-water temperature recorded after the measurement on Core 204-1246B-5H (Fig. F27), we suspect that APCT 12, which was used for all of these measurements, suddenly recalibrated itself during the second measurement. This observation led us to calibrate all of the APCT tools in an ice bath. Tools were placed in a trash can full of ice for at least 35 min. Results indicated serious calibration problems and are shown in Figure F26. A “corrected” temperature gradient for Site 1246 was calculated by assuming that APCT 12 required no correction for the first measurement and a correction of +2.5°C for the rest of the measurements (Fig. F26). This assumption leads to a temperature gradient that is consistent with other sites. APCT 12 was taken out of service, and APCT 11 was used for the rest of the leg. Comparison of data from APCTs 12 and 11 at Site 1244 suggests that APCT 12 was well calibrated prior to this unprecedented spontaneous recalibration (see “Downhole Tools and Pressure Coring,” p. 29, in the “Site 1244” chapter).

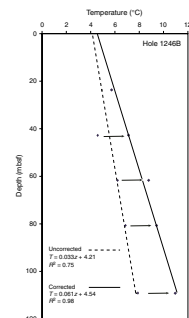
T13. Shear strength data, p. 66.

T14. Temperature measurements, p. 67.

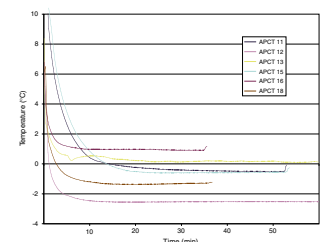
F25. Raw data for estimating in situ temperatures, p. 47.



F26. Subsurface temperatures plotted vs. depth, p. 48.



F27. Temperatures recorded during APCT tool calibration, p. 49.



In Situ Pressure Measurements

No in situ pressure measurements were made at this site.

Pressure Core Sampler

No PCS cores were taken at this site.

HYACINTH Pressure Core Sampling

No HYACINTH pressure cores were taken at this site.

DOWNHOLE LOGGING

Logging While Drilling

Operations

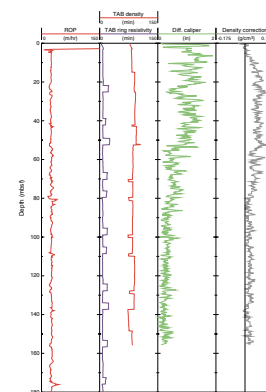
LWD at Site 1246 began at 0830 hr Universal Time Coordinated (UTC) on 19 July 2002 by spudding Hole 1246A at 861.50 meters below rig floor (mbrf) water depth (drillers depth) on the northeastern flank of Hydrate Ridge. The LWD tools (6³/₄-in collars) included the Geo Vision Resistivity (GVR) resistivity-at-the-bit (RAB) tool with 9¹/₈-in button sleeve, the MWD (Powerpulse), the NMR-MRP tool, and the Vision Neutron Density (VND) tool. Drilling proceeded at ~25 m/hr to TD at 180 mbsf without difficulty, and real-time data were transmitted to the surface to evaluate formation properties. Two stands of drill pipe were pulled up from the bottom of the hole without rotating (sliding test) to evaluate the effects of drilling on the NMR-MRP tool. Tools were pulled to the rig floor at 0300 hr UTC on 20 July, and the data from Holes 1245A and 1246A were downloaded. The total bit run was ~19 hr.

Logging Quality

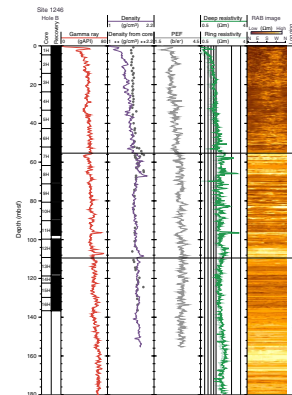
Figure F28 shows the quality control logs for Hole 1246A. The target rate of penetration (ROP) of 25 m/hr (± 5 m/hr) was generally achieved, although some large variations in ROP were observed just below the seafloor. The measured ROP was sufficient to record one sample per 4-cm interval (~25 samples per meter) and was obtained over 94% of the total section of the hole. The quality of RAB images is thus quite high, and no significant resolution loss is observed with variation in ROP at Hole 1246A. However, the quality of the RAB images in the upper 50 mbsf of Hole 1246A (Fig. F29) is degraded by an apparent problem associated with low rates of bit rotation. The NMR-MRP tool porosity data were enhanced by using a slow drilling rate, resulting in a sampling resolution of approximately one sample per every 15-cm interval.

The differential caliper log (DCAL), which gives the distance between the tool sensor and the wall of the borehole as recorded by the LWD density tool, is the best indicator of borehole conditions. The DCAL values are >1 in over the uppermost 50 mbsf of the hole, showing wash-outs that have degraded the near-surface LWD data. The density correction (DRHO) (calculated from the difference between the short- and long-spaced density measurements) varies from 0 to 0.14 g/cm³ (Fig. F28), which shows the generally good quality of the density measurements. A standoff of <1 in between the tool and the borehole wall

F28. LWD logs, p. 50.



F29. LWD data, p. 51.



indicates high-quality density measurements with an accuracy of ± 0.018 g/cm³.

Time-after-bit (TAB) measurements are 10 ± 2 min for ring resistivity and gamma ray logs and 89 ± 5 min for density and neutron porosity logs (Fig. F28). TAB values remain relatively constant, coinciding with steady ROP while drilling.

The depths, relative to seafloor, for all of the logs were fixed by identifying the gamma ray signal associated with the seafloor and shifting the logging data to the appropriate depth as determined by the drillers pipe tallies. For Hole 1246A, it was determined that the gamma ray log pick for the seafloor was at a depth of 859.0 mbrf. The rig floor logging datum was located 10.9 m above sea level for this hole.

Interpretation of Logging-While-Drilling Logging

Data from Hole 1246A show excellent quality LWD logs. The presence of gas hydrate was identified from ~55 to 109 mbsf by high resistivities and RAB image anomalies, allowing quantitative estimates of gas hydrate saturations. Within the zone of expected gas hydrate stability (above a depth of ~114 mbsf), the RAB image reveals several conspicuous high-resistivity zones that appear to be gas hydrate-bearing intervals. Low to high gamma ray and density logging measured interbedding throughout Hole 1246A that may indicate lithologic changes associated with turbidites and/or the presence of free gas below the GHSZ.

Logging Units

The logged section in Hole 1246A is divided into three “logging units” on the basis of obvious changes in the LWD gamma ray, density, and electrical resistivity measurements (Fig. F29).

Logging Unit 1 (0–55 mbsf) is characterized by increasing resistivities and densities with depth as measured by the LWD tools. However, this trend in the downhole logging data is probably in part a result of degraded logging measurements within the enlarged portion of the borehole near the surface as shown in Figure F28. Logging Unit 1 includes all of lithostratigraphic Unit I (0–21 mbsf) and the upper portion of lithostratigraphic Unit II (21–138 mbsf), which are composed of clay to silty clay sediments (see “**Lithostratigraphic Unit II,**” p. 3, in “Lithostratigraphic Unit” in “Lithostratigraphy”). The transition from logging Unit 1 to logging Unit 2 is defined by a significant increase in electrical resistivity from ~0.8 to >1.6 Ω m. The density and gamma ray logs also reveal a pronounced change at the contact between logging Unit 1 and 2, with an increase in the LWD recorded densities and gamma ray values of >0.3 g/cm³ and 10 American Petroleum Institute gamma ray units (gAPI), respectively.

Logging Unit 2 (55–109 mbsf) is characterized by zones of distinct high resistivities, with peak resistivity values >2 Ω m. The gamma ray log in this unit shows a characteristic cyclicity of values that may reflect the interbedded sand and clay turbidite sequences as described by the shipboard sedimentologists for lithostratigraphic Unit II (21–137 mbsf) (see “**Lithostratigraphic Unit II,**” p. 3, in “Lithostratigraphic Unit” in “Lithostratigraphy”). The downhole logging-measured densities in Unit 2 reveal several conspicuous high-density intervals within the depth interval from 55 to 68 mbsf and from 103 to 109 mbsf, with peak values exceeding 2.0 g/cm³. These two anomalous intervals likely represent

the regionally described seismic Horizon B (~60 mbsf) and Horizon B' (~100 mbsf) (see “**Lithostratigraphy**,” p. 2). Because of the lack of acoustic transit-time logging data from Site 1246, the RAB resistivity logging image has been used to select the depth of the boundary between logging Units 2 and 3, which is marked by a drop in the recorded borehole resistivity with depth. Also noted on the density log is a subtle drop in density at the contact between Unit 2 and 3, which roughly corresponds to the depth of the BSR at this site.

Logging Unit 3 (109–180 mbsf; TD of Hole 1246A) corresponds to the lower part of lithostratigraphic Unit II (21–138 mbsf), which is described as an interbedded sand, silt, and silty-clay turbidite sequence. Logging Unit 3 is generally characterized by lower and more uniform resistivities compared to Unit 2.

Logging Porosities

Sediment porosities can be determined from analyses of recovered cores and from numerous borehole measurements (see “**Physical Properties**,” p. 22, and “**Downhole Logging**,” p. 43, both in the “Explanatory Notes” chapter). Data from the LWD density, neutron, and NMR-MRP logs have been used to calculate sediment porosities for Hole 1246A. Core-derived physical property data, including porosities (see “**Physical Properties**,” p. 10), have been used to both calibrate and evaluate the log-derived sediment porosities.

The VND LWD-derived measurements of density in Hole 1246A (Fig. F29) generally increase with depth, with values averaging ~1.4 g/cm³ near the seafloor to >1.8 g/cm³ at the bottom of logging Unit 3. The density logging measurements are degraded in logging Unit 1 as discussed above. The LWD log-derived density measurements from Hole 1246A were used to calculate sediment porosities (ϕ) using the standard density-porosity relation:

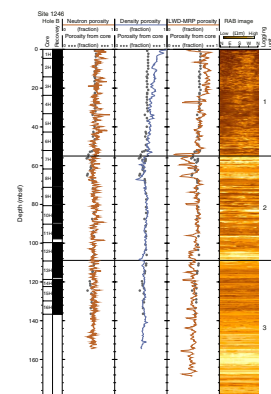
$$\phi = (\rho_m - \rho_b) / (\rho_m - \rho_w).$$

Water density (ρ_w) was assumed to be constant and equal to 1.05 g/cm³; however, variable core-derived grain/matrix densities (ρ_m) were assumed for each logging density porosity calculation. The core-derived grain densities (ρ_m) from Hole 1246B ranged from an average value at the seafloor of 2.71 to ~2.69 g/cm³ at the bottom of the hole (see “**Physical Properties**,” p. 10). The density log-derived porosities in logging Units 1–3 (0–180 mbsf) of Hole 1246A range from ~40% to 80% (Fig. F30).

The LWD neutron porosity log from Hole 1246A (Fig. F30) yielded sediment porosities ranging from an average value at the top of the logged section of ~70% to ~60% in logging Unit 3. The “total” sediment porosities derived by the NMR-MRP tool in Hole 1224A (Fig. F30) ranged from ~80% near the seafloor to ~50% near the bottom of the hole.

In studies of downhole logging data, it is common to combine and compare porosity data from different sources to evaluate results and assess the accuracy of a particular measurement. The comparison of core-derived and log-derived porosities in Figure F30 reveals that the density-derived porosities are generally similar to the core porosities in logging Units 2 and 3 from Hole 1246A. However, the LWD density-derived porosities are generally higher than the core-derived porosities in Unit 1. At the top of logging Unit 2, the LWD density log also appears to be ~3 m deeper than the core-derived densities. This offset is

F30. LWD- and core-derived porosities, p. 52.



best explained by local variability in the geology of this site, with Hole 1246A (LWD hole) being drilled more than 80 m west of Hole 1246B (core hole). The neutron porosities are slightly higher than the core-derived porosities throughout most of the hole. The NMR-MRP tool porosities are generally lower than the core-derived porosities in logging Units 2 through 3. The NMR-MRP tool porosities in logging Unit 1 (above ~25 mbsf) appear to have been significantly degraded by washouts in the upper part of the hole. The NMR-MRP tool porosity log also exhibits numerous low-porosity zones throughout the entire hole, which will be further evaluated after the cruise.

Gas Hydrate

The presence of gas hydrate at Site 1246 was documented by several strong IR anomalies in Hole 1246B at depths of 66.45, 96.64, 104.93, 105.08, and 109.20 mbsf. Despite the limited presence of gas hydrates, it was inferred, based on geochemical pore water analyses (see “**Interstitial Water Geochemistry**,” p. 7), IR image analysis of cores (see “**Physical Properties**,” p. 10), and downhole logging data that disseminated gas hydrate is present in portions of logging Unit 2. As previously discussed in “**Downhole Logging**,” p. 43, in the “Explanatory Notes” chapter, the presence of gas hydrate is generally characterized by increases in logging-measured electrical resistivities and acoustic velocities. Logging Unit 2 at Site 1246 is characterized by a distinct stepwise increase in electrical resistivities, but we have no acoustic data (because no wireline logging was conducted at Site 1246) to further evaluate the presence of gas hydrate or free gas at this site. One of the most notable appearances of gas hydrate at Site 1246 was imaged by the RAB tool in Hole 1246A at a depth of 96–97 mbsf. The presence of gas hydrate was also inferred in Hole 1246B at a depth of 96.64 mbsf based on IR anomaly data. The shipboard sedimentologists have described this interval as a volcanic glass-bearing horizon in the cores from Hole 1246B (Horizon B’ at a depth ~100 mbsf) (see “**Lithostratigraphy**,” p. 2). The LWD resistivity tool also reveals several thin high-resistivity zones within logging Unit 1 (0–55 mbsf), which may suggest the possible presence of gas hydrate.

Resistivity logging data have been used to quantify the amount of gas hydrate at Site 1246. For the purpose of discussion, it is assumed that the high electrical resistivities measured in logging Unit 2 are due to the presence of gas hydrate. The Archie Relation,

$$S_w = (aR_w/\phi^m R_t)^{1/n}$$

(see “**Electrical Resistivity**,” p. 59, in “Downhole Logging” in the “Explanatory Notes” chapter), was used with resistivity data (R_t) from the LWD RAB tool and porosity data (ϕ^m) from the LWD density tool to calculate water saturations in Hole 1246A. It should be noted that gas hydrate saturation (S_h) is the measurement of the percentage of pore space in sediment occupied by gas hydrate, which is the mathematical complement of the Archie-derived S_w , with

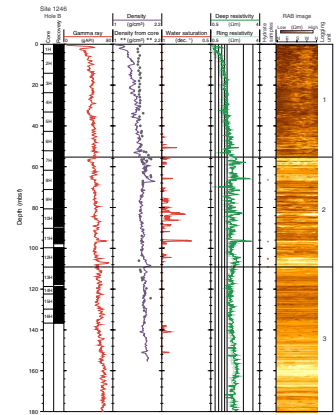
$$S_h = 1 - S_w$$

For the Archie Relation, the formation water resistivity (R_w) was calculated from recovered core water samples and the Archie a and m vari-

ables were calculated by a crossplot technique that compares the downhole logging-derived resistivities and density porosities. See Collett and Ladd (2000) for the details on how to calculate the required formation water resistivities and Archie variables. The values used for Site 1246 were $a = 1$, $m = 2.8$, and $n = 1.9386$.

The Archie Relation yielded water saturations (Fig. F31) ranging from an average minimum value of ~70% to a maximum of 100% in logging Unit 2 (55–109 mbsf) of Hole 1246A, which implies the gas hydrate saturations in logging Unit 2 range from 0% to 30%. It also appears that logging Unit 1 may contain several thin gas hydrate-bearing intervals. The low water saturations shown in logging Unit 3 within the depth interval from ~138 to 153 mbsf, which are below the zone of potential gas hydrate stability, may indicate the presence of free gas-bearing sediments.

F31. Logging-derived gas hydrate saturations, p. 53.



REFERENCES

- Clague, D., Maher, N., and Paull, C.K., 2001. High-resolution multibeam survey of Hydrate Ridge, offshore Oregon. In Paul, C.K., and Dillon, W.P. (Eds.), *Natural Gas Hydrates: Occurrence, Distribution, and Detection*. Am. Geophys. Union, Geophys. Monogr. Ser., 124:297–306.
- Collett, T.S., and Ladd, J., 2000. Detection of gas hydrate with downhole logs and assessment of gas hydrate concentrations (saturations) and gas volumes on the Blake Ridge with electrical resistivity log data. In Paull, C.K., Matsumoto, R., Wallace, P.J., and Dillon, W.P. (Eds.), *Proc. ODP, Sci. Results*, 164: College Station, TX (Ocean Drilling Program), 179–191.
- Dallimore, S.R., Uchida, T., and Collett, T.S. (Eds.), 1999. *Scientific Results from JAPEX/JNOC/GSC Mallik 2L-38 Gas Hydrate Research Well, MacKenzie Delta, Northwest Territories Canada*. Bull.—Geol. Surv. Canada.
- Edmond, J.M., Measures, C., McDuff, R.E., Chan, L.H., Collier, R., and Grant, B., 1979. Ridge crest hydrothermal activity and the balances of the major and minor elements in the ocean: the Galapagos data. *Earth Planet. Sci. Lett.*, 46:1–18.
- Kastner, M., Kvenvolden, K.A., Whiticar, M.J., Camerlenghi, A., and Lorenson, T.D., 1995. Relation between pore fluid chemistry and gas hydrates associated with bottom-simulating reflectors at the Cascadia Margin, Sites 889 and 892. In Carson, B., Westbrook, G.K., Musgrave, R.J., and Suess, E. (Eds.), *Proc. ODP, Sci. Results*, 146 (Pt 1): College Station, TX (Ocean Drilling Program), 175–187.
- Lee, M.W., and Dillon, W.P., 2001. Amplitude blanking related to gas hydrate concentration. *Mar. Geophys. Res.*, 22:101–109.
- Pujos-Lamy, A., 1977a. *Emiliana* et *Gephyrocapsa* (Nannoplankton calcaire): biometrie et interet biostratigraphique dans le Pleistocene superieur marin des Acores. *Rev. Esp. Micropaleontol.*, 9:69–84.
- Pujos-Lamy, A., 1977b. Essai d'établissement d'une biostratigraphie du nannoplankton calcaire dans le Pleistocene de l'Atlantique Nord-oriental. *Boreas*, 6:323–331.
- Seyfried, W.E., Jr., Janecky, D.R., and Mottl, M.J., 1984. Alteration of the oceanic crust: implications for geochemical cycles of lithium and boron. *Geochim. Cosmochim. Acta*, 48:557–569.

Figure F1. Bathymetric map showing locations of holes drilled at Site 1246. Bathymetry from EM300 data acquired by Monterey Bay Aquarium Research Institute (MBARI) (Clague et al., 2001).

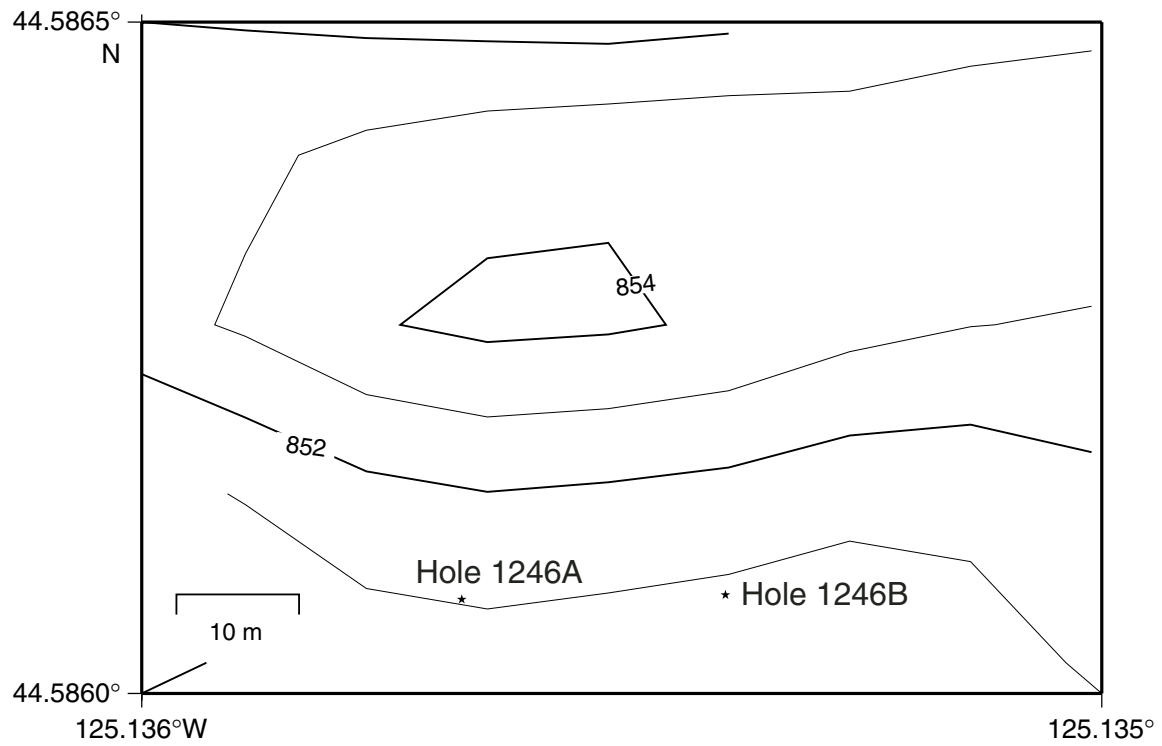


Figure F2. Lithostratigraphic summary for Site 1246.

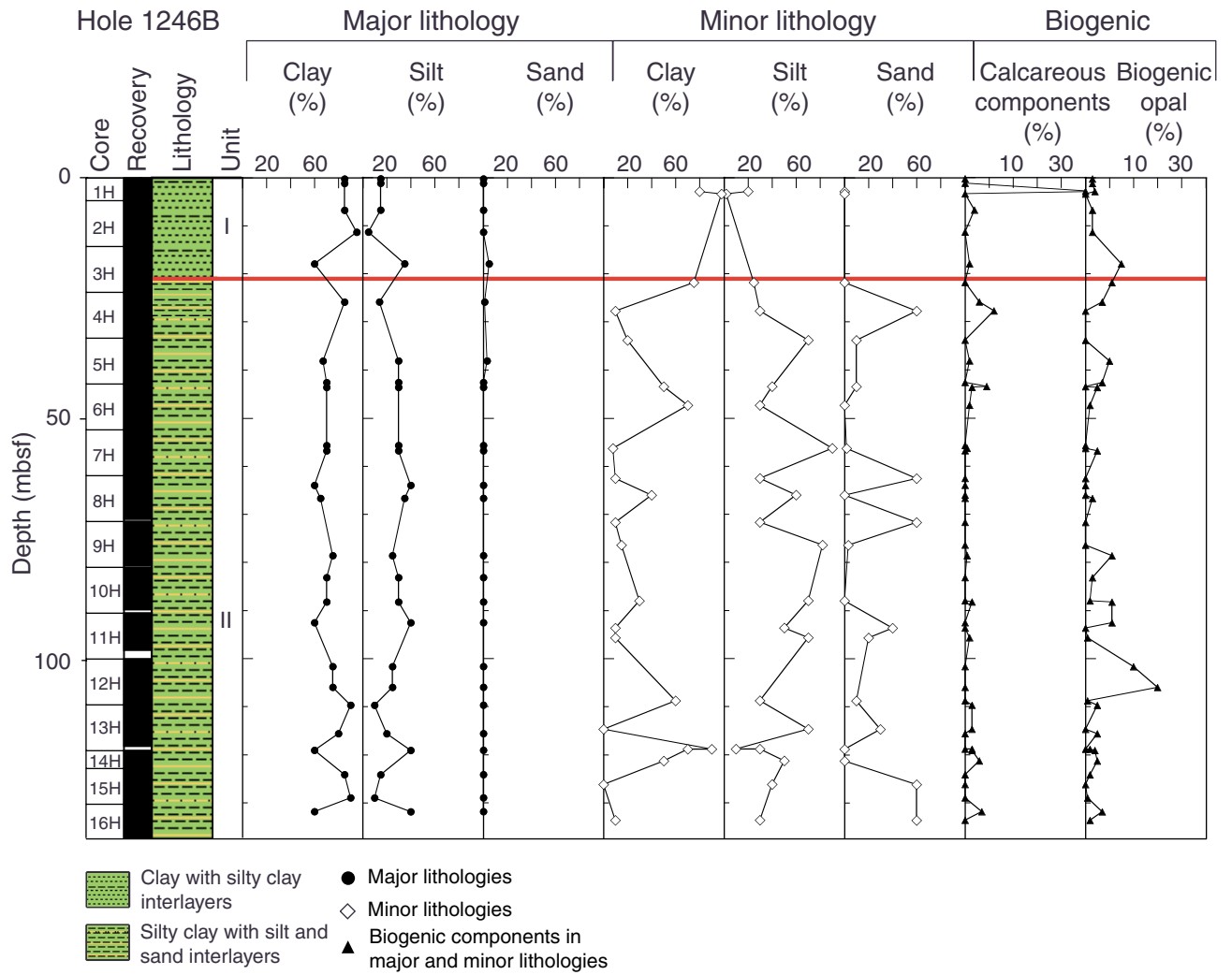


Figure F3. A portion of an east-west seismic reflection profile from the 3-D seismic survey at Site 1246. LWD density and ring resistivity (Res_ring) data, lithostratigraphic unit boundaries, seismic Horizons B and B', and the bottom-simulating reflector (BSR) are shown. SF = seafloor.

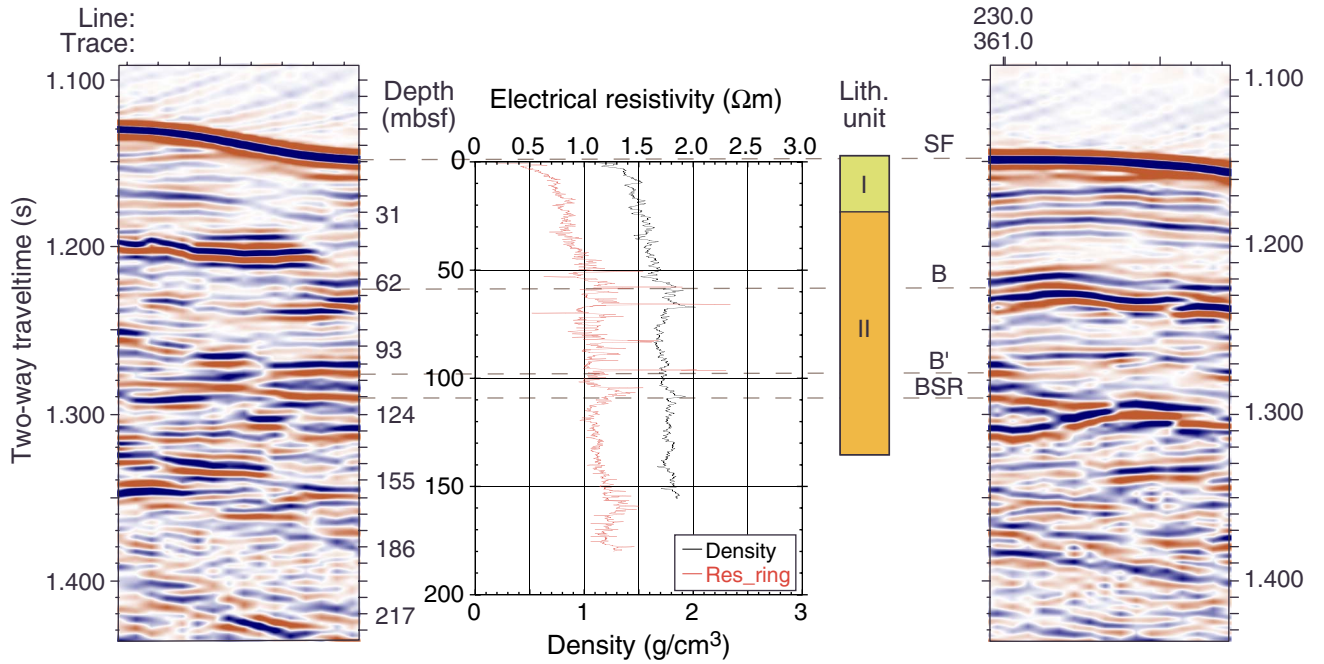
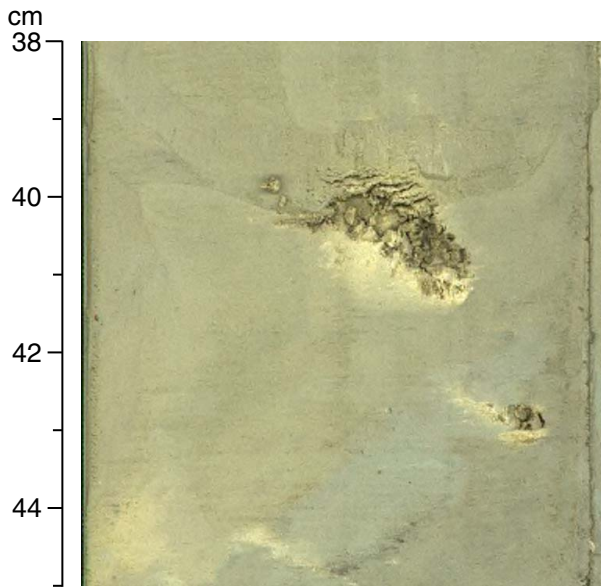


Figure F4. A. Close-up photograph of light-colored crumbly authigenic carbonate observed in Sample 204-1246B-1H-3, 38–45 cm. B. Smear slide photomicrograph (crossed nicols; Sample 204-1246B-1H-3, 40 cm) from the carbonate above. Note the tabular calcite crystals of high birefringence.

A



B

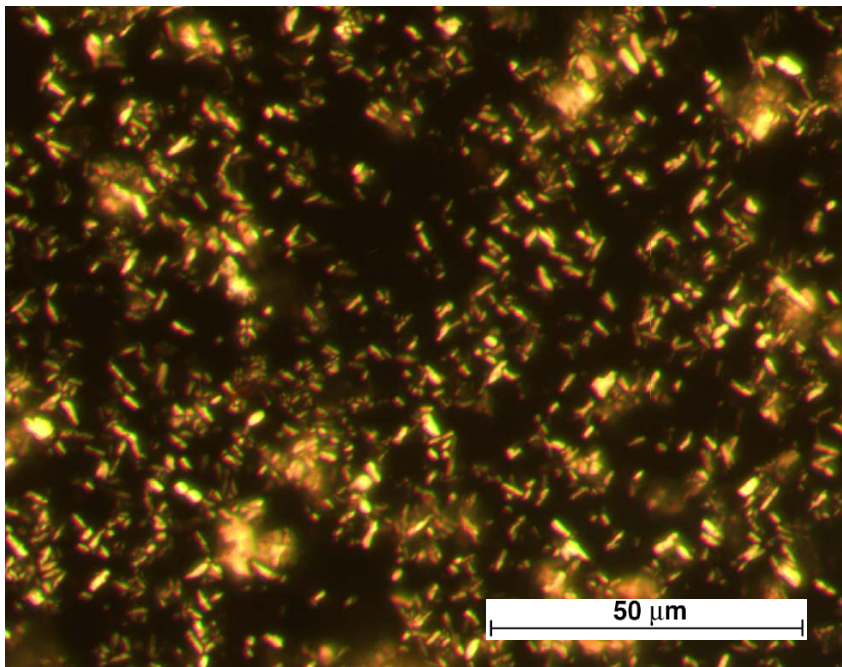


Figure F5. A. Close-up photograph of volcanic glass-rich horizons (interval 204-1246B-10H-5, 123–132 cm). B. Interval 204-1246B-11H-4, 92–102 cm.

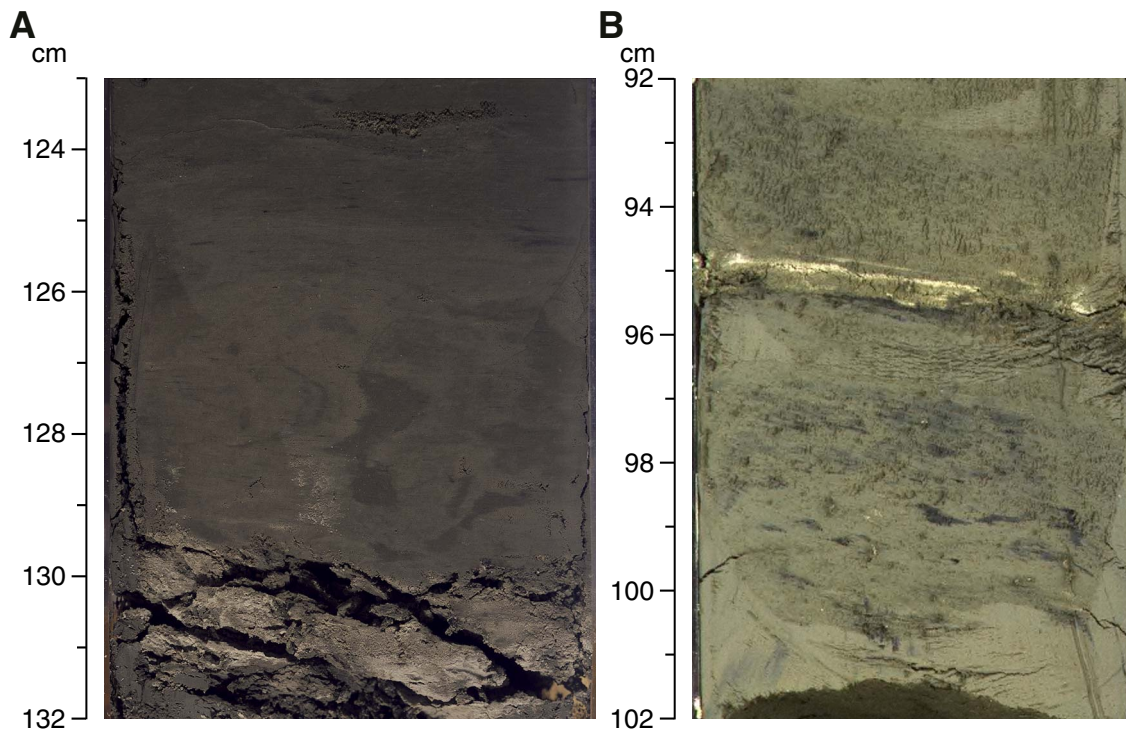


Figure F6. Photomicrograph of volcanic glass shards seen in a smear slide (Sample [204-1246B-10H-5](#), 131 cm).

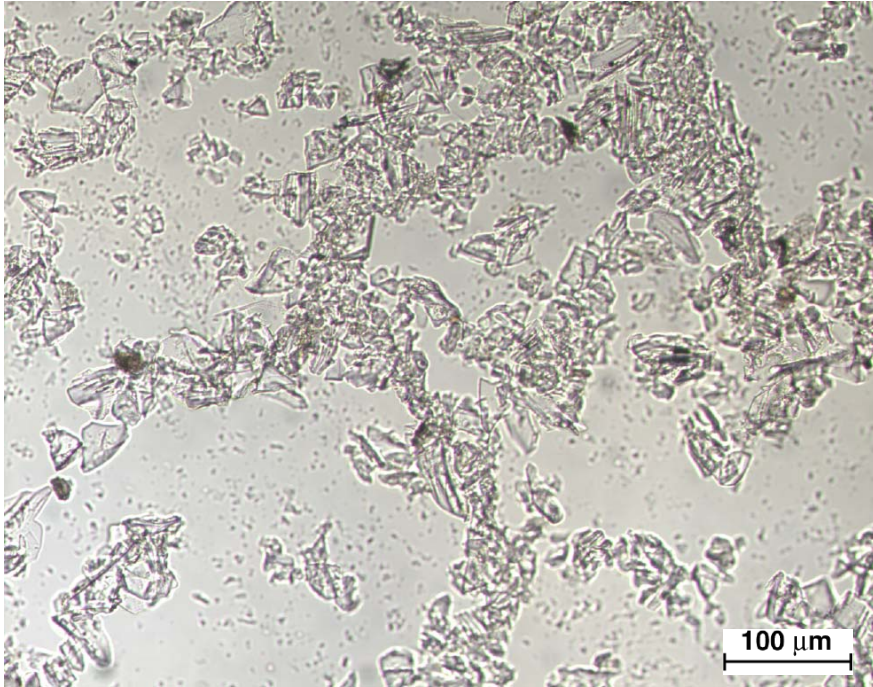


Figure F7. Age-depth plots based on diatom and calcareous nannofossil bioevents from Hole 1246B. The detailed age and depth of control points are shown in Table T2, p. 55. D = diatom event, N = nannofossil event.

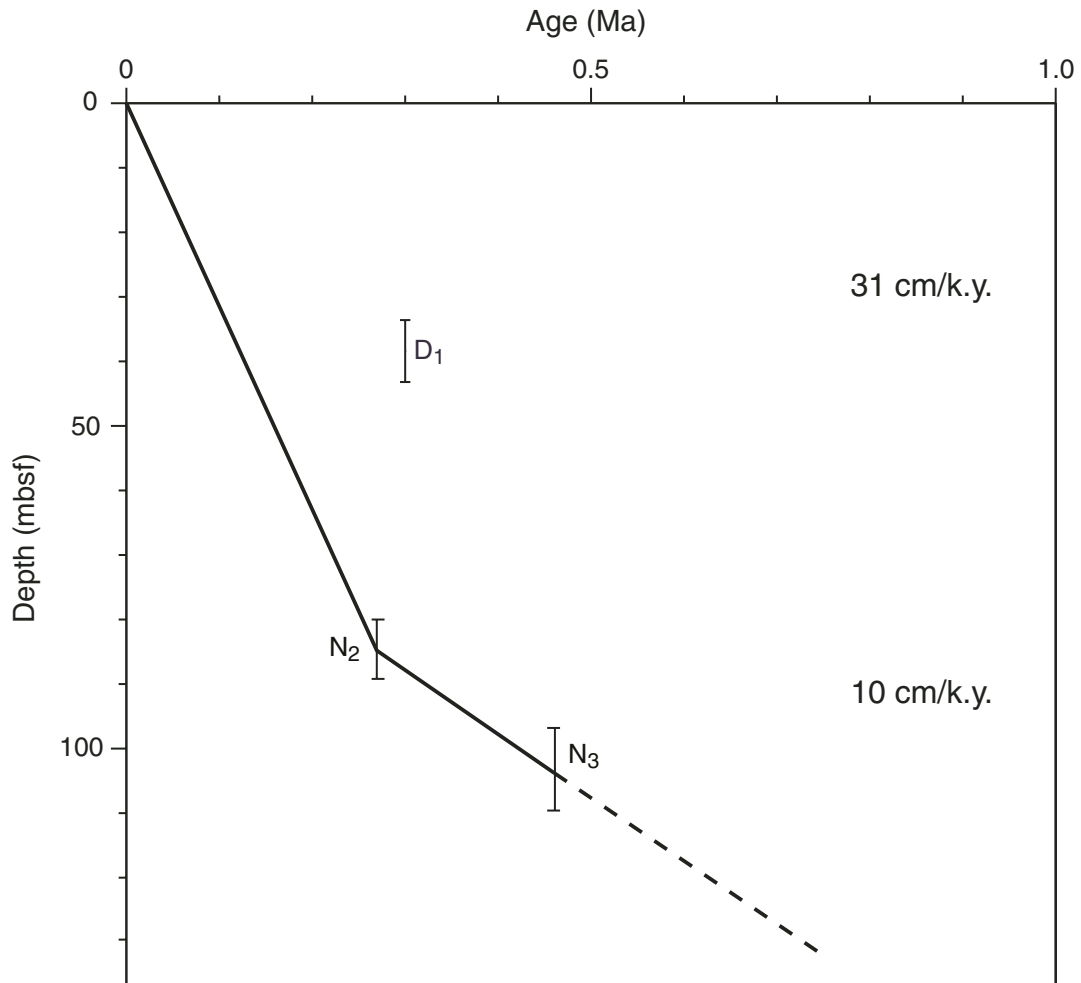


Figure F8. Concentration profiles of various dissolved species in pore water from Hole 1246B. DOC = dissolved organic carbon. (Continued on next page.)

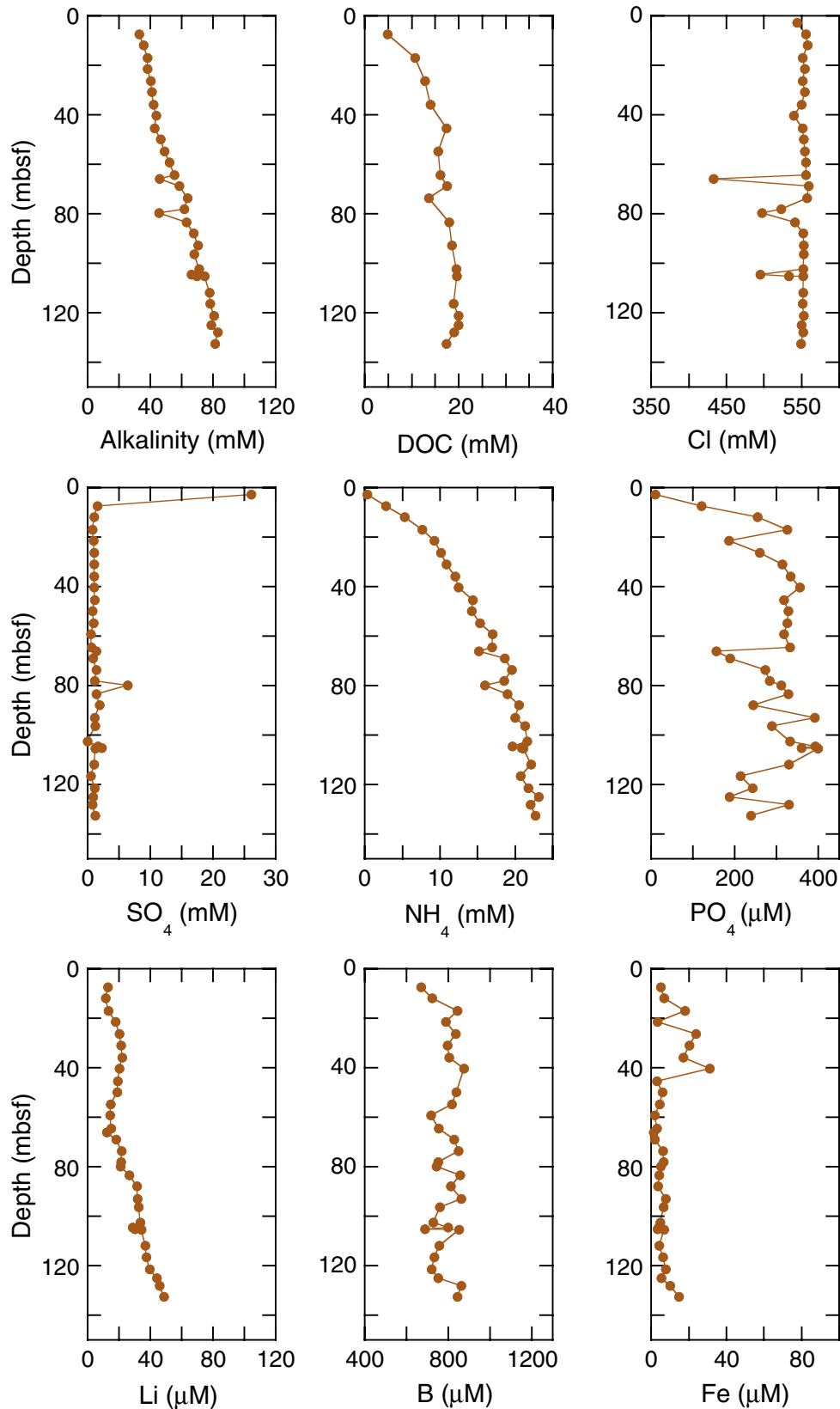


Figure F8 (continued).

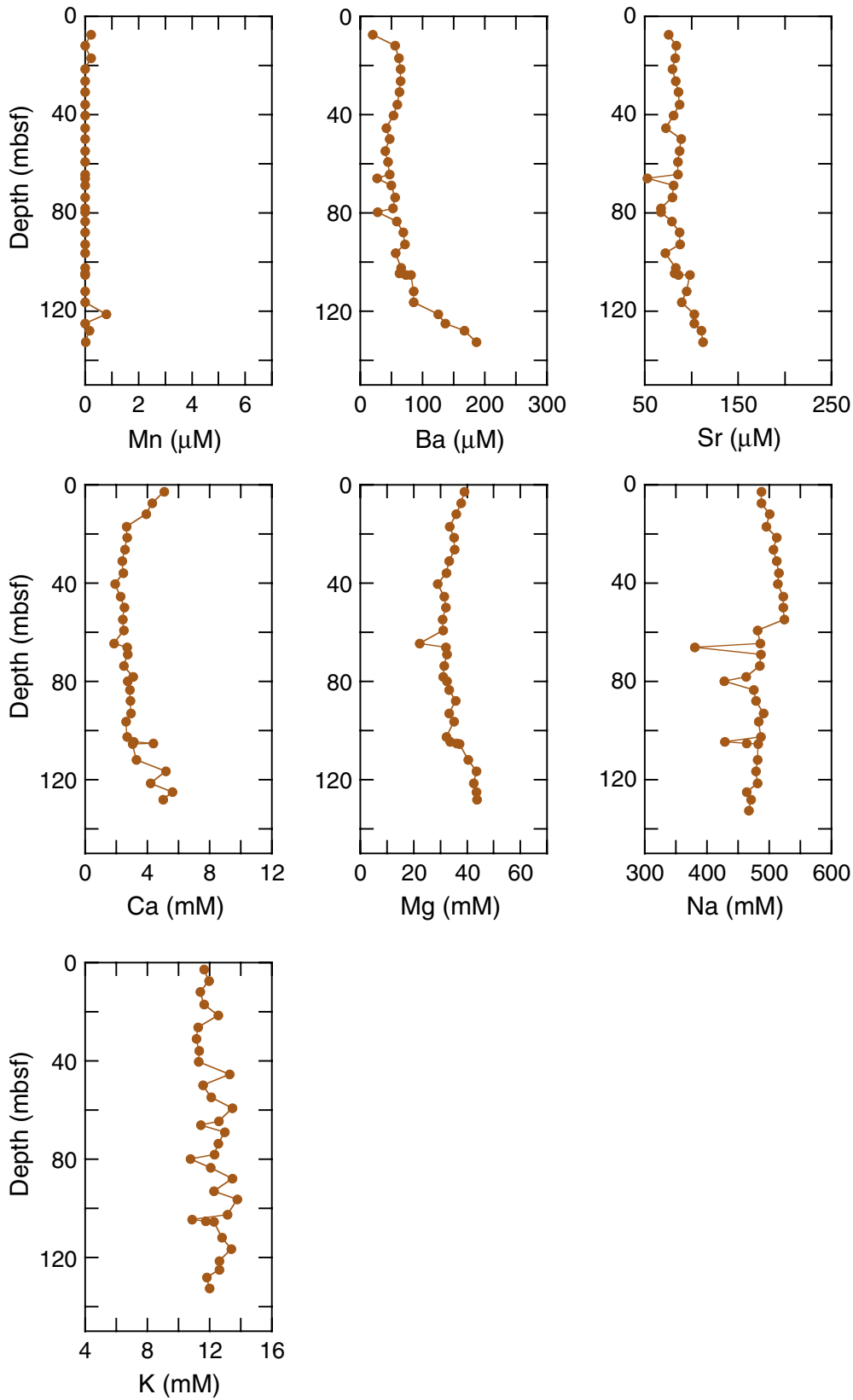


Figure F9. A. Cl^- concentration data from Site 1246, showing excursions to fresher values superimposed on a near-vertical baseline and the position of the bottom-simulating reflector (BSR). Interstitial Cl^- data from Site 1244 (dotted blue lines) are shown for comparison. B. Estimates of the fraction of pore space occupied by gas hydrate at Sites 1246 (red circles) and 1244 (blue circles) from the available IW data.

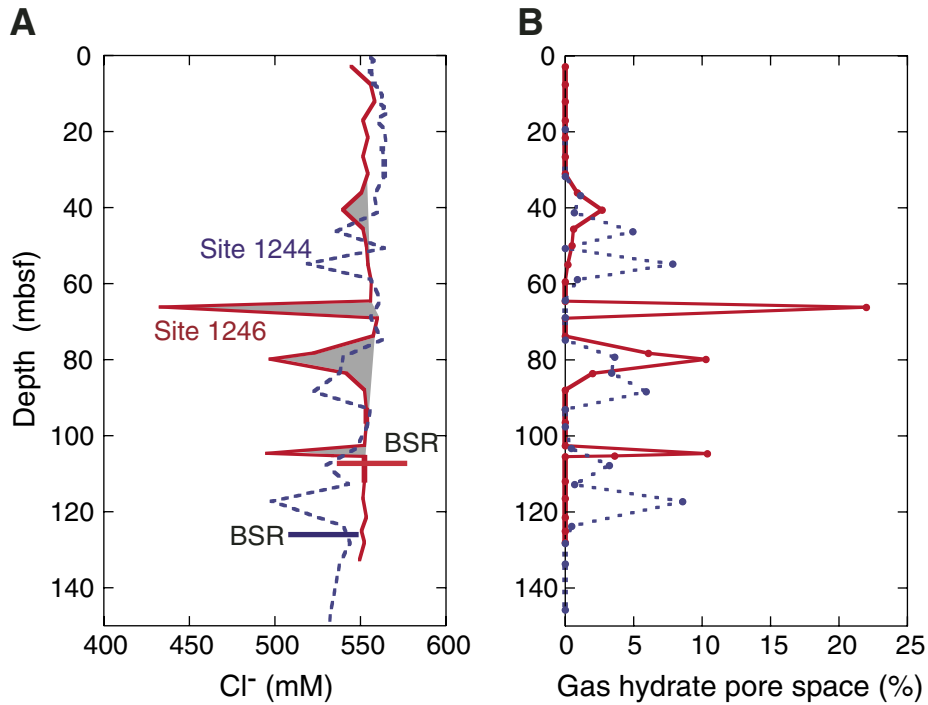


Figure F10. Interstitial dissolved lithium (Li^+) concentration at Site 1246 compared with the distribution for Site 1244. At both sites, the sediment interval corresponding to the seismic reflection denoted as Horizon B (see "Introduction," p. 1) corresponds to a marked decrease in the dissolved lithium content. BSR = bottom-simulating reflector.

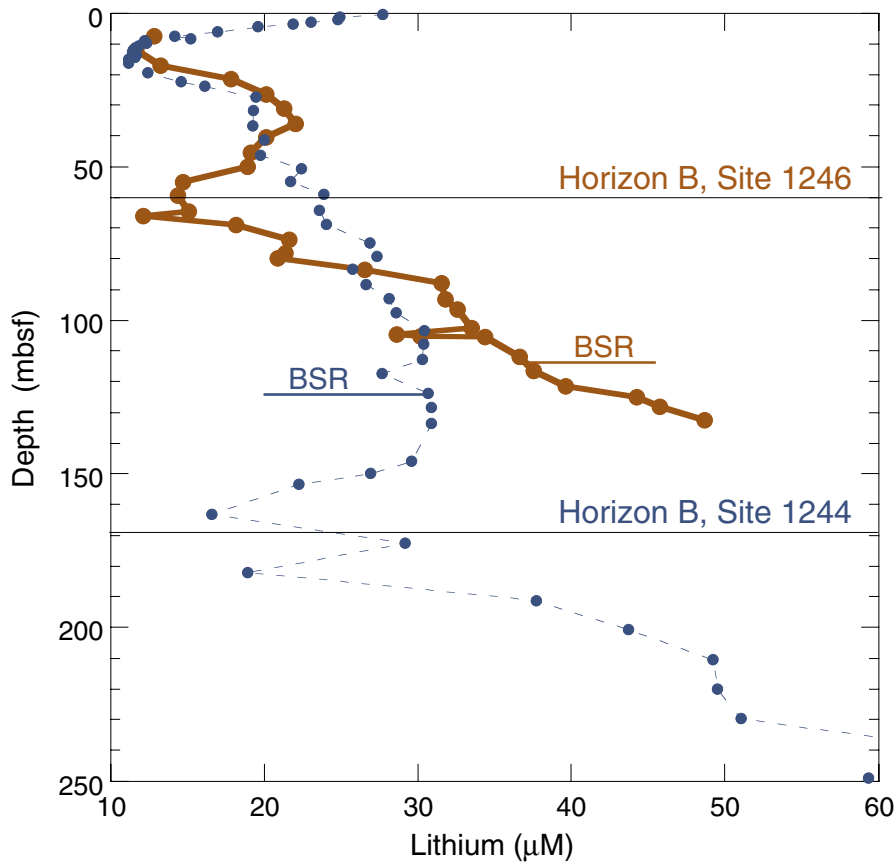


Figure F11. Profiles of iron showing the increase in the concentration of this element presumably at the depth where dissolved sulfide is consumed at Sites 1246 (red circles) and 1244 (blue circles).

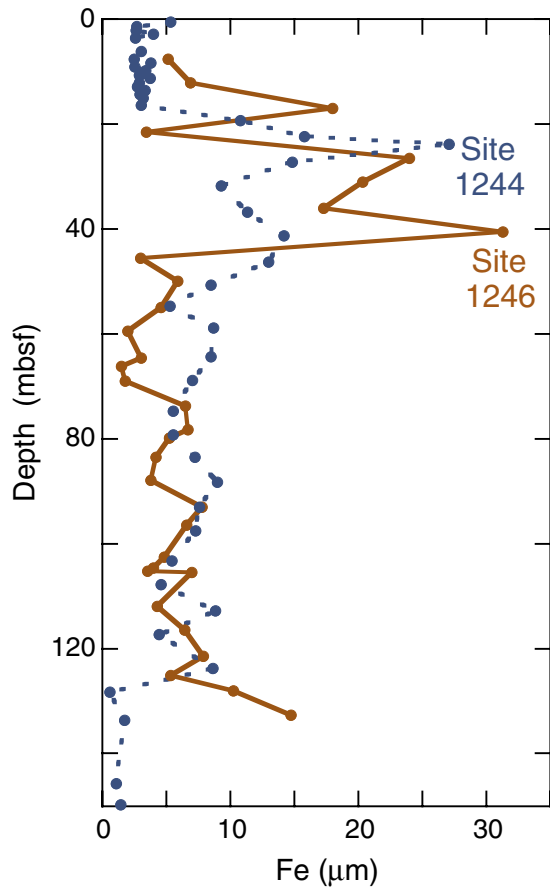


Figure F12. Headspace gas concentrations of C_1 , C_2 , $C_{2=}$, and C_3 vs. depth for Site 1246.

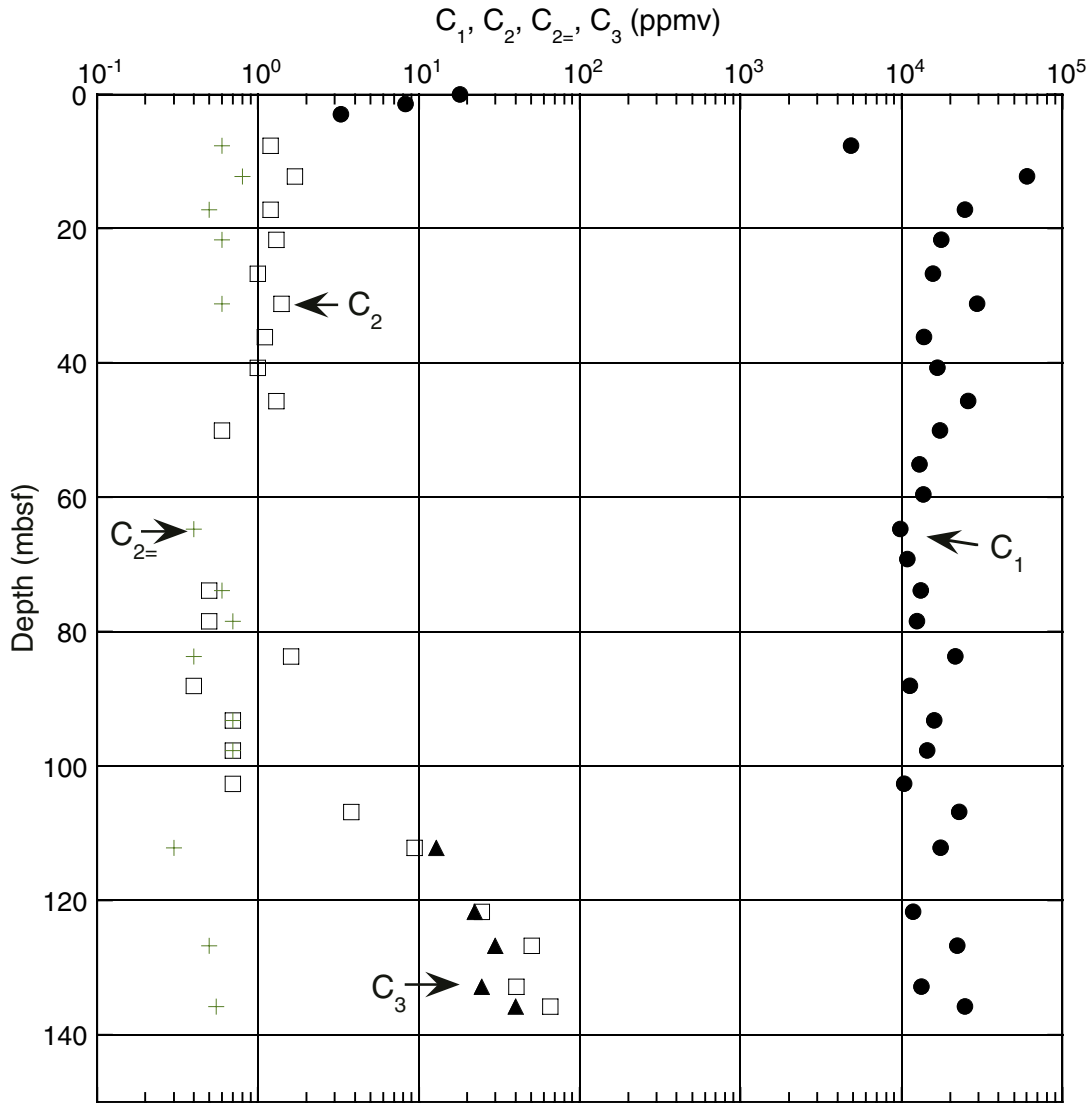


Figure F13. Dissolved residual methane (CH_4) and sulfate (SO_4^{2-}) in pore water. The methane concentration increases at the depth where the sulfate concentration is depleted.

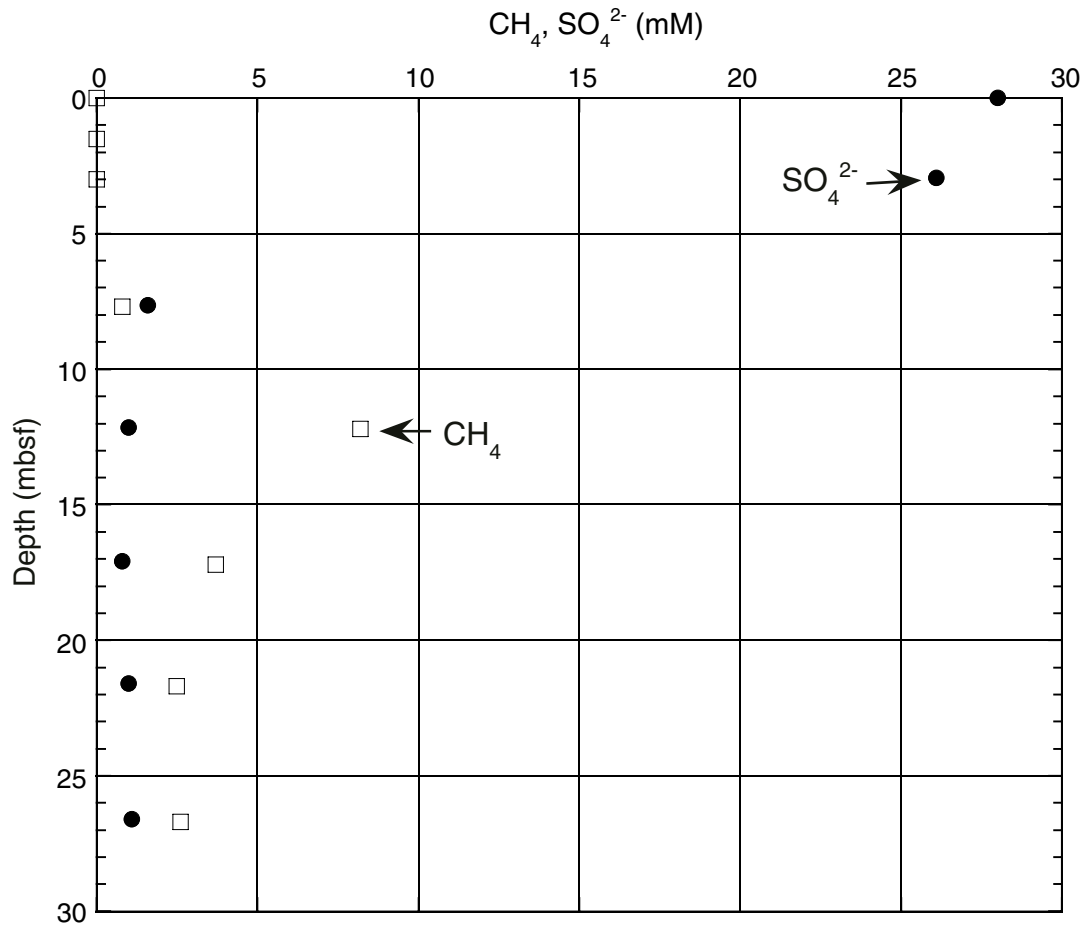


Figure F14. Concentrations of C_1 , C_2 , C_3 , and $i-C_4$ in core void gas vs. depth from Site 1246.

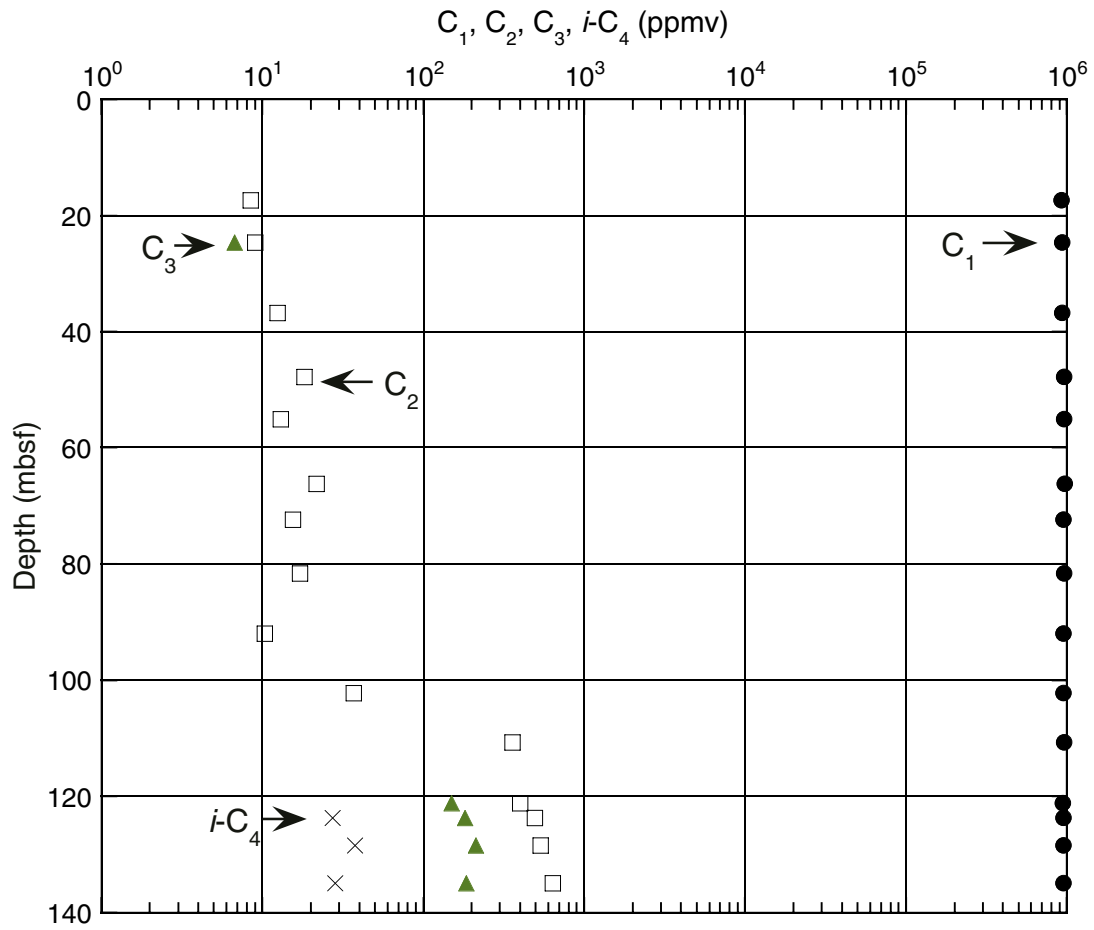


Figure F15. C_1/C_2 ratio vs. depth at Site 1246. VAC = void gas (vacutainer), HS = headspace gas.

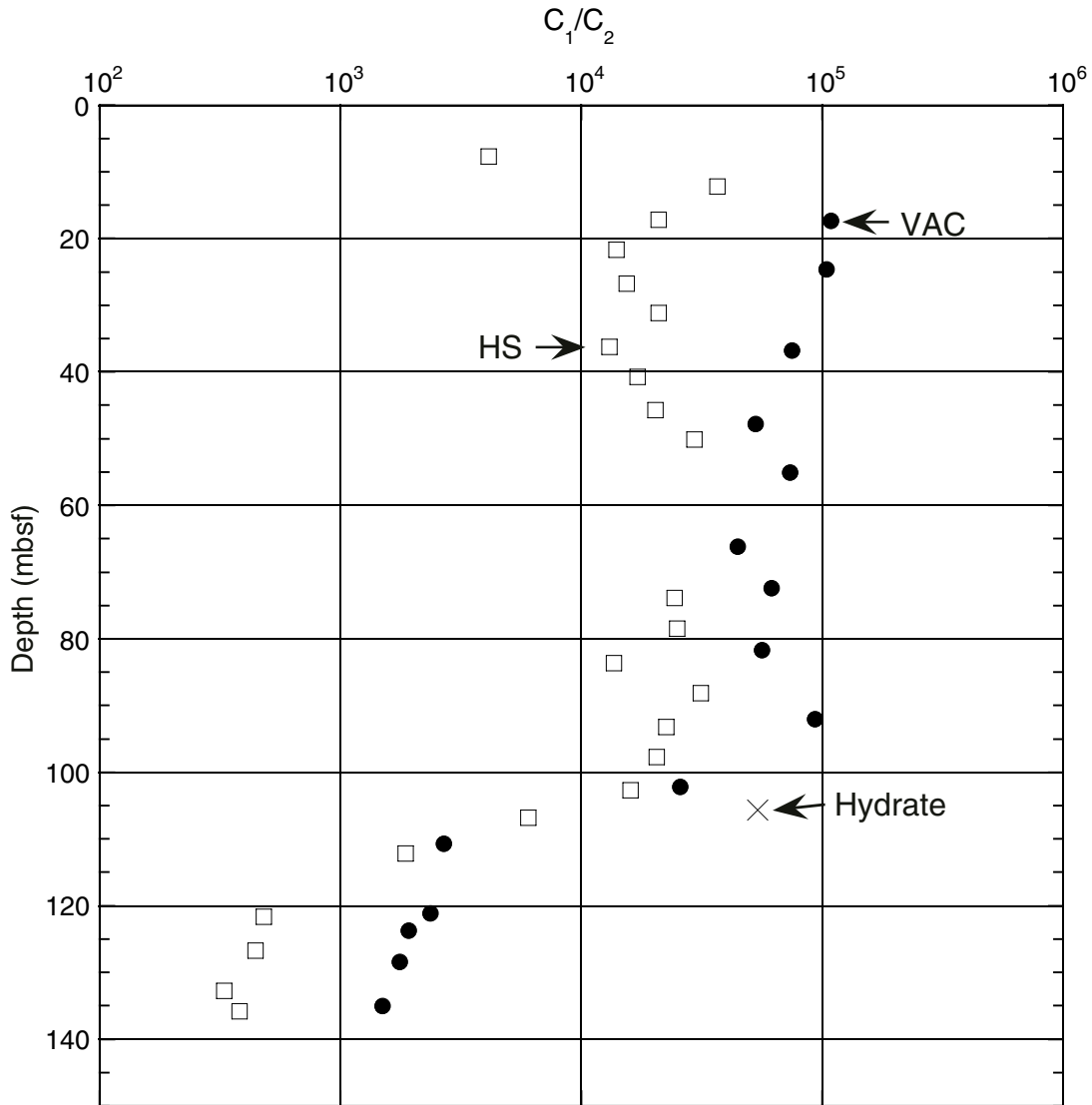


Figure F16. Downcore variation in carbonate carbon (IC), organic carbon (OC), total nitrogen (TN), total sulfur (TS), and C/N ratios in sediment from Site 1246.

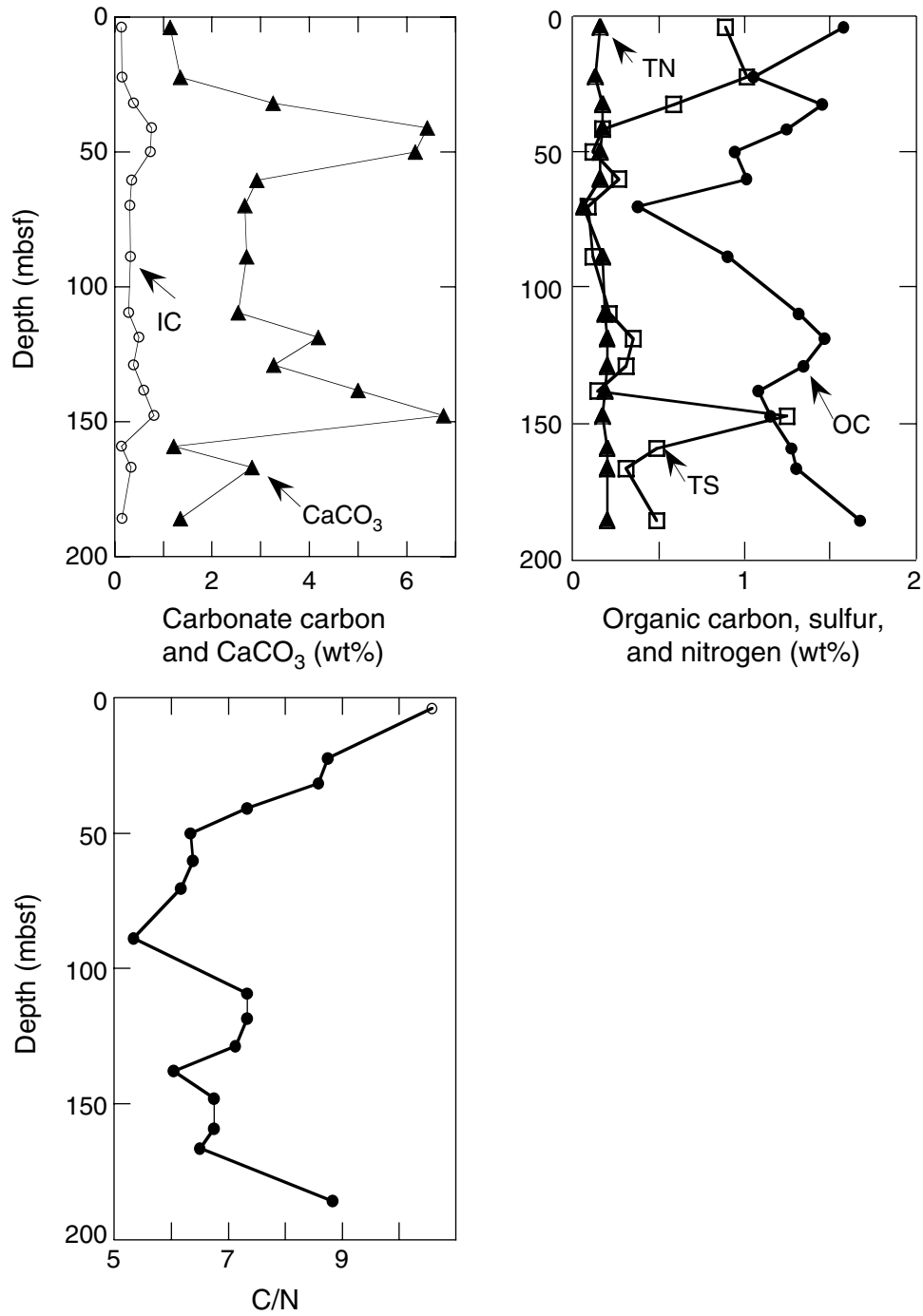


Figure F17. Downcore temperature from IR images from Hole 1246B. BSR = bottom-simulating reflector.

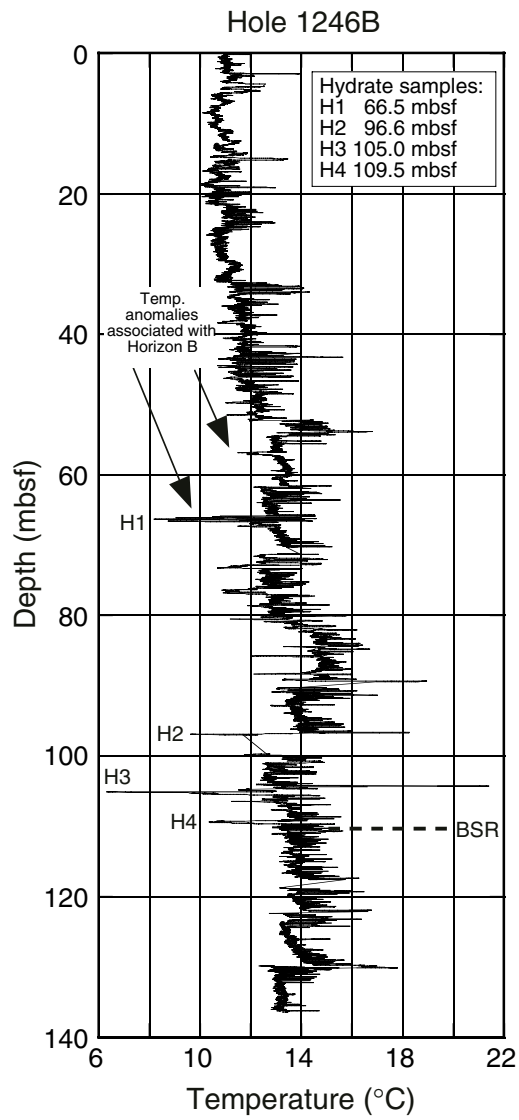


Figure F18. Comparison of IR anomalies and S_w derived from LWD resistivity from Hole 1246B. Resistivity data are plotted in terms of apparent S_w using Archie's Relation; the estimated hydrate concentration is 1.0 – S_w (see "Downhole Logging," p. 15).

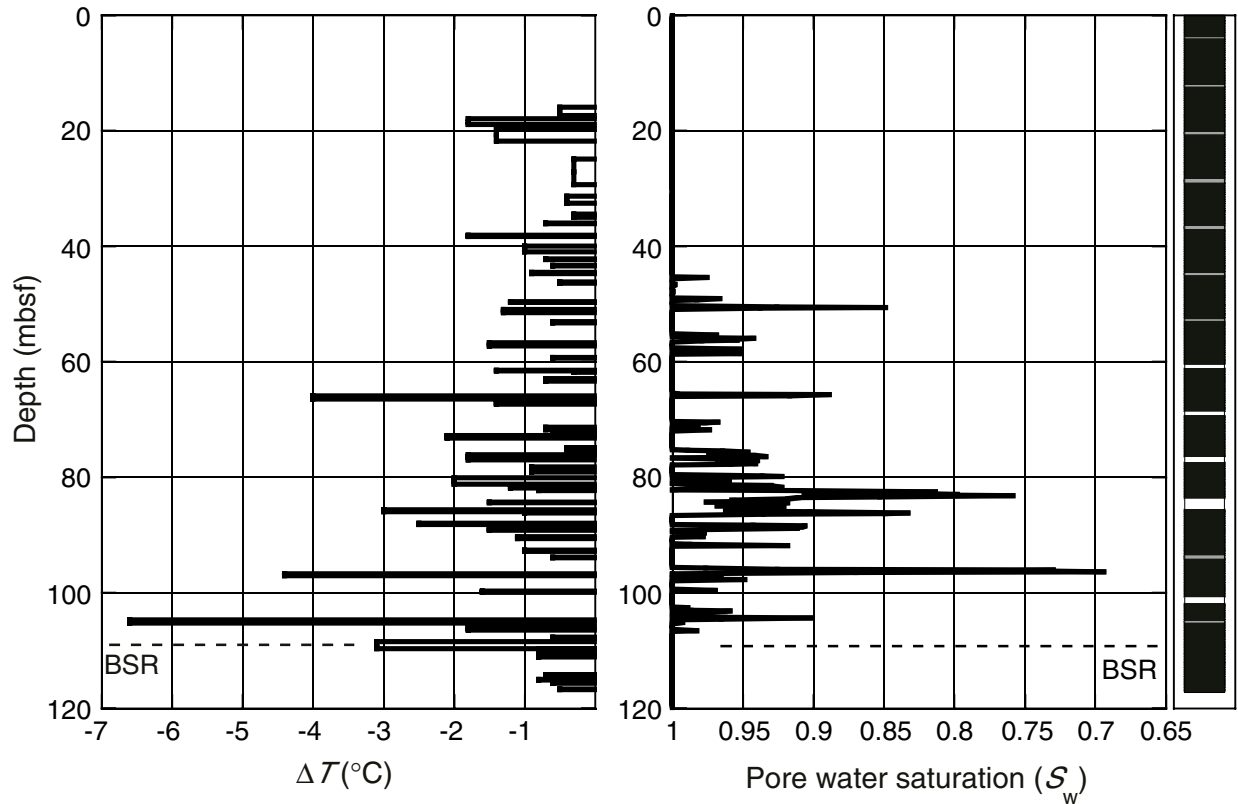


Figure F19. Detailed comparison of the hydrate anomaly at 66 mbsf (Core 204-1246-8H) in Hole 1246B before curation. The individual temperature anomalies correspond well with the extracted temperature profile. The total cold-spot anomaly is ~0.5 m long if the voids are removed.

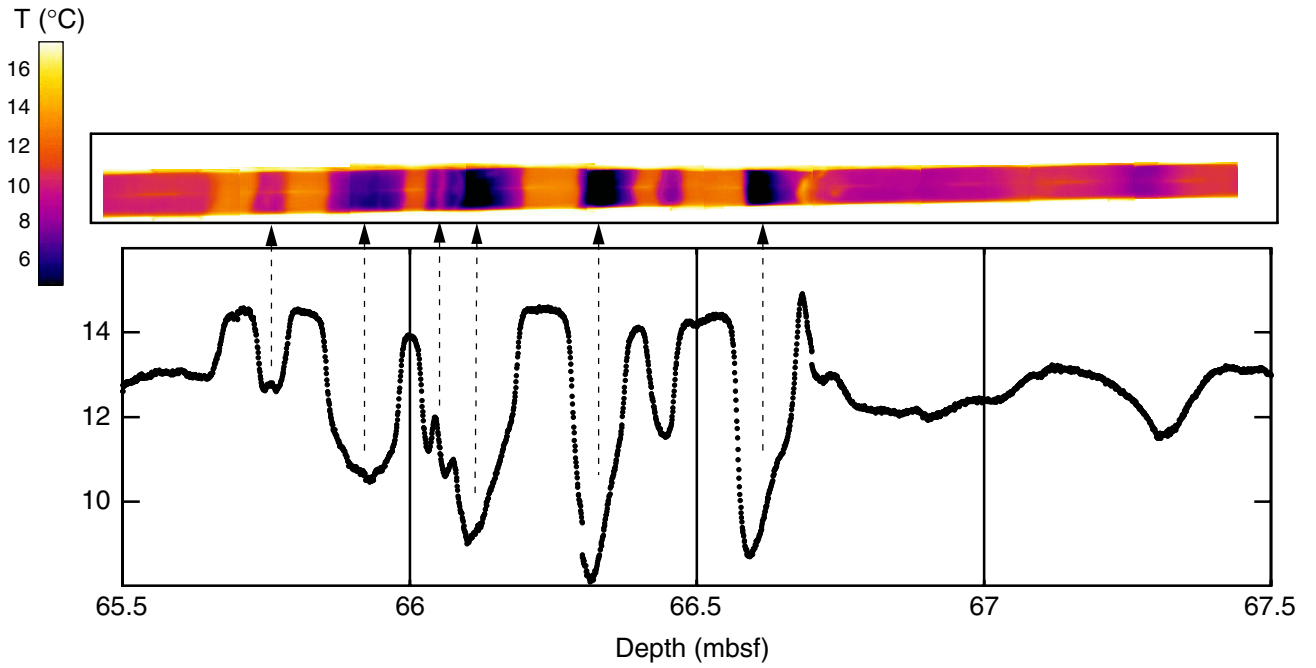


Figure F20. Physical properties including bulk density from logging while drilling (LWD), gamma ray attenuation (GRA), moisture and density (MAD) bulk density, porosity, grain density, magnetic susceptibility, thermal conductivity, and shear strength data at Site 1248. ASV = automated shear vane, TV = Torvane.

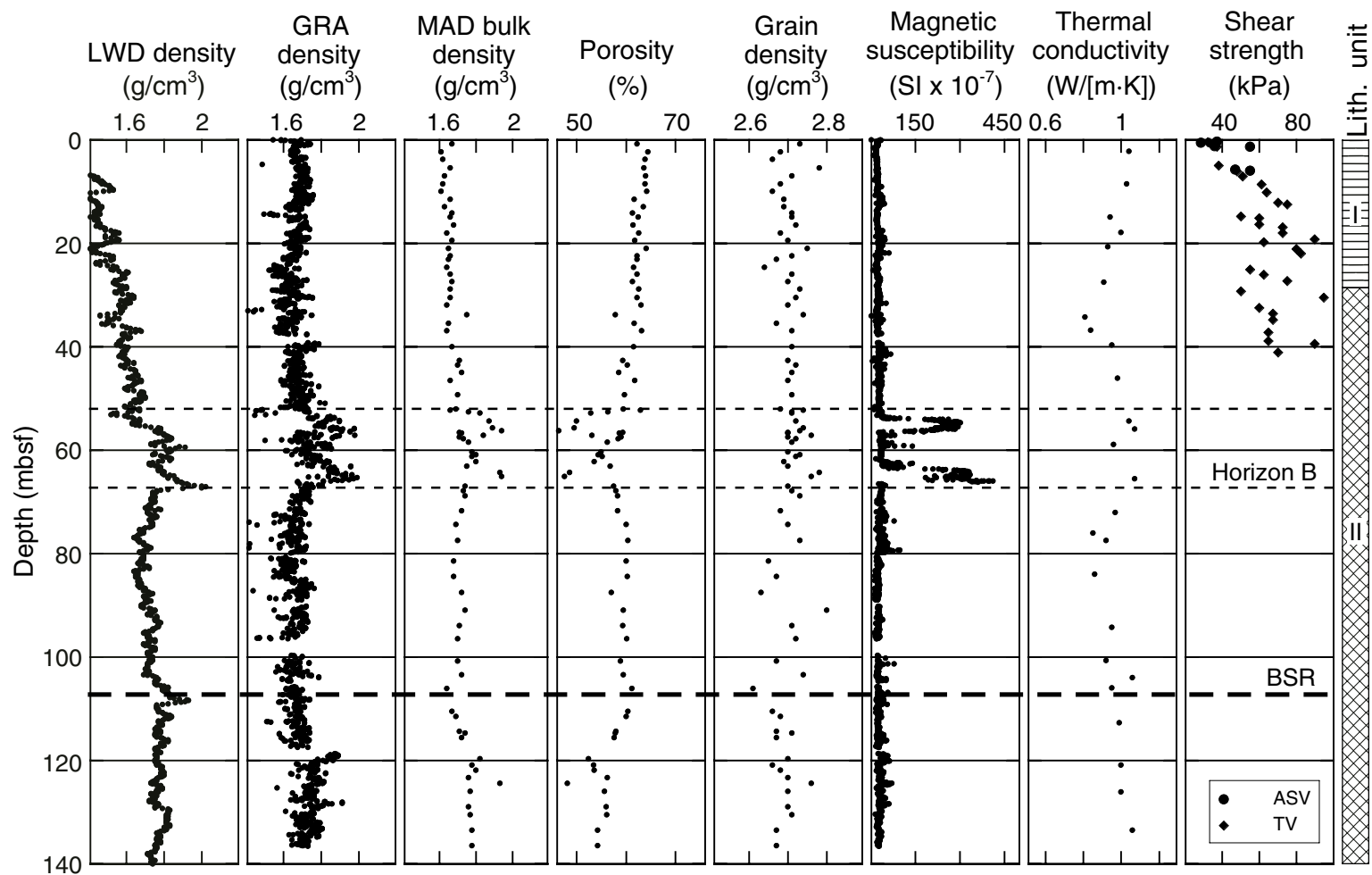


Figure F21. Correlation between physical properties and the seismic record at Site 1246. GRA = Gamma ray attenuation, MAD = moisture and density, BSR = bottom-simulating reflector.

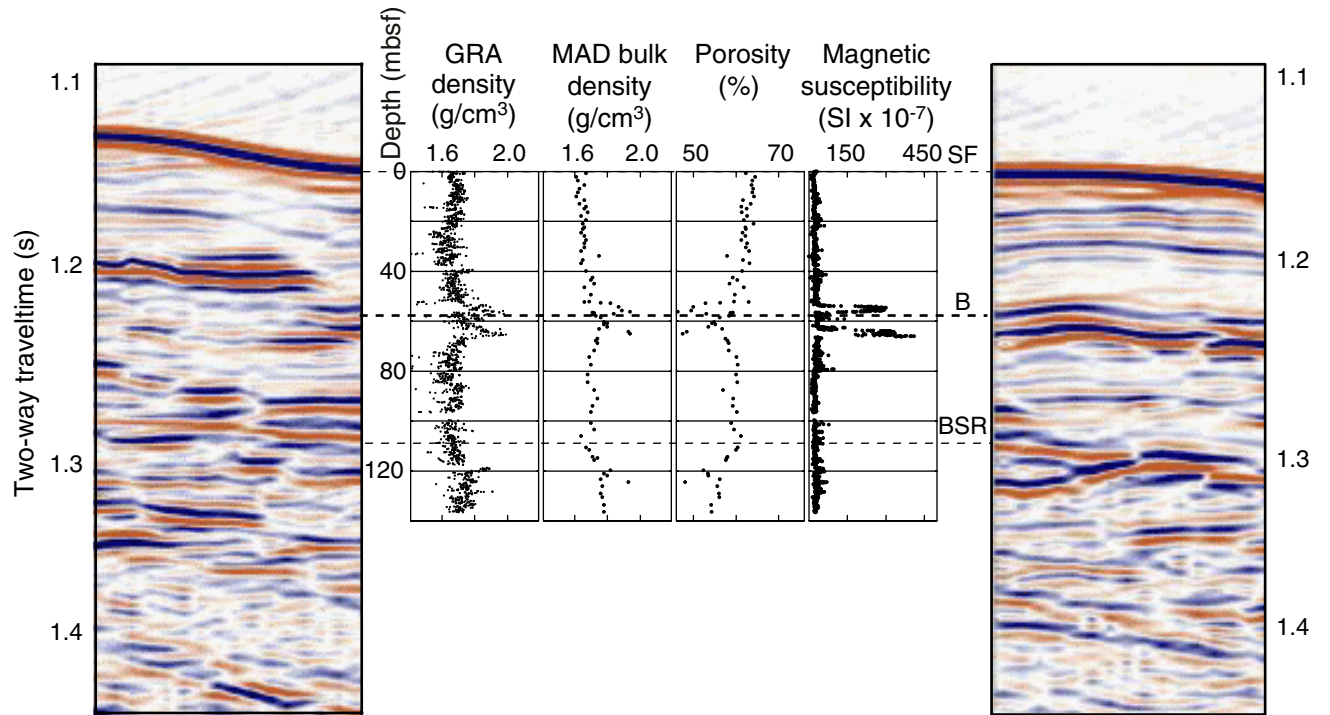


Figure F22. A. Comparison of sedimentology and physical properties for MS Event 1 within Horizon B at 55 mbsf (Core 204-1246B-7H). LWD = logging-while-drilling, GRA =gamma ray attenuation. (Continued on next page.)

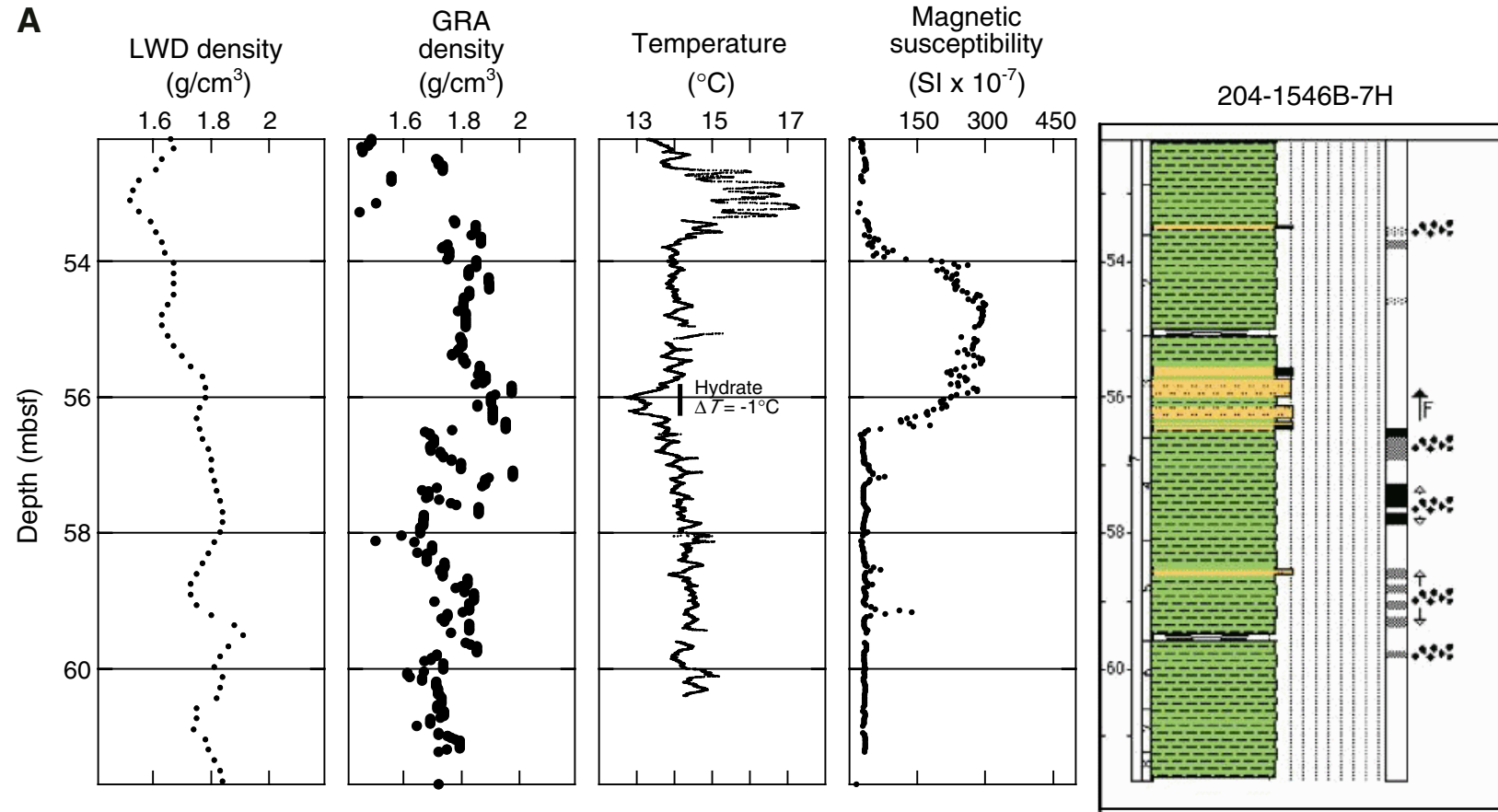


Figure F22 (continued). B. Comparison of sedimentology and physical properties for MS Event 2 within Horizon B at 66 mbsf (Core 204-1246B-8H). Compare to Figure F19, p. 40, for details in temperature anomaly. See Figure F3, p. 70, in the “Explanatory Notes” chapter for the sedimentology key. LWD = logging-while-drilling, GRA =gamma ray attenuation.

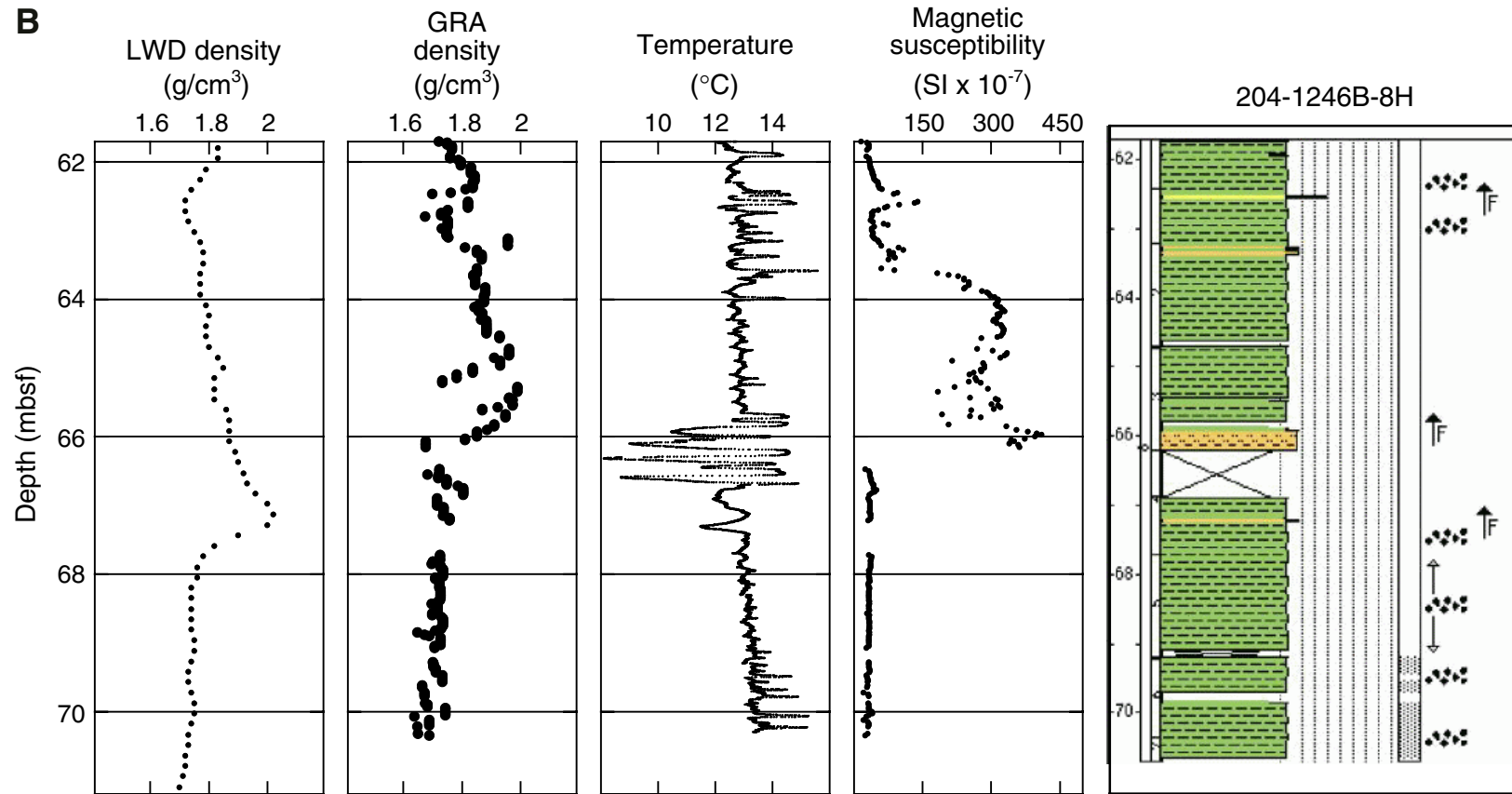


Figure F23. Downhole measurements of noncontact resistivity (NCR) mainly dominated by gas expansion cracks (high resistivity) in Hole 1246B.

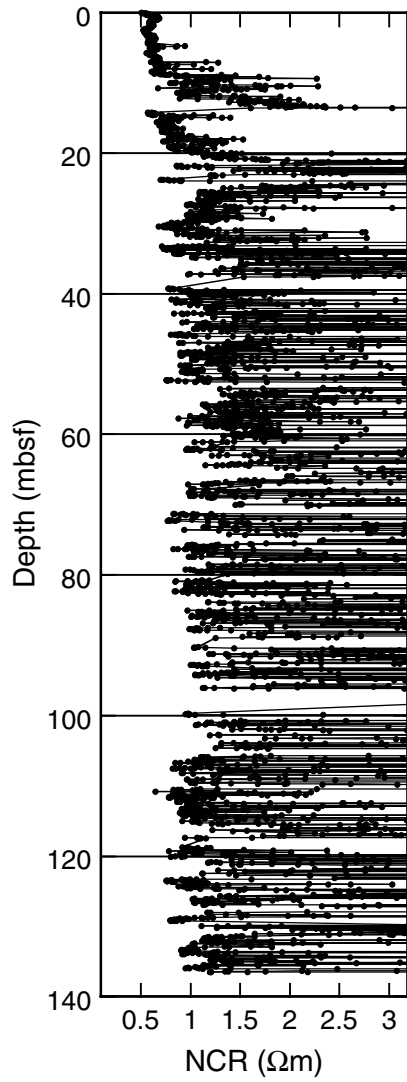


Figure F24. Comparison of V_p in the upper 10 mbsf with noncontact resistivity and bulk density at Site 1246. The V_p shows a small anisotropy because of sedimentation-related bedding. GRA = gamma ray attenuation, MAD = moisture and density, MST = multisensor track.

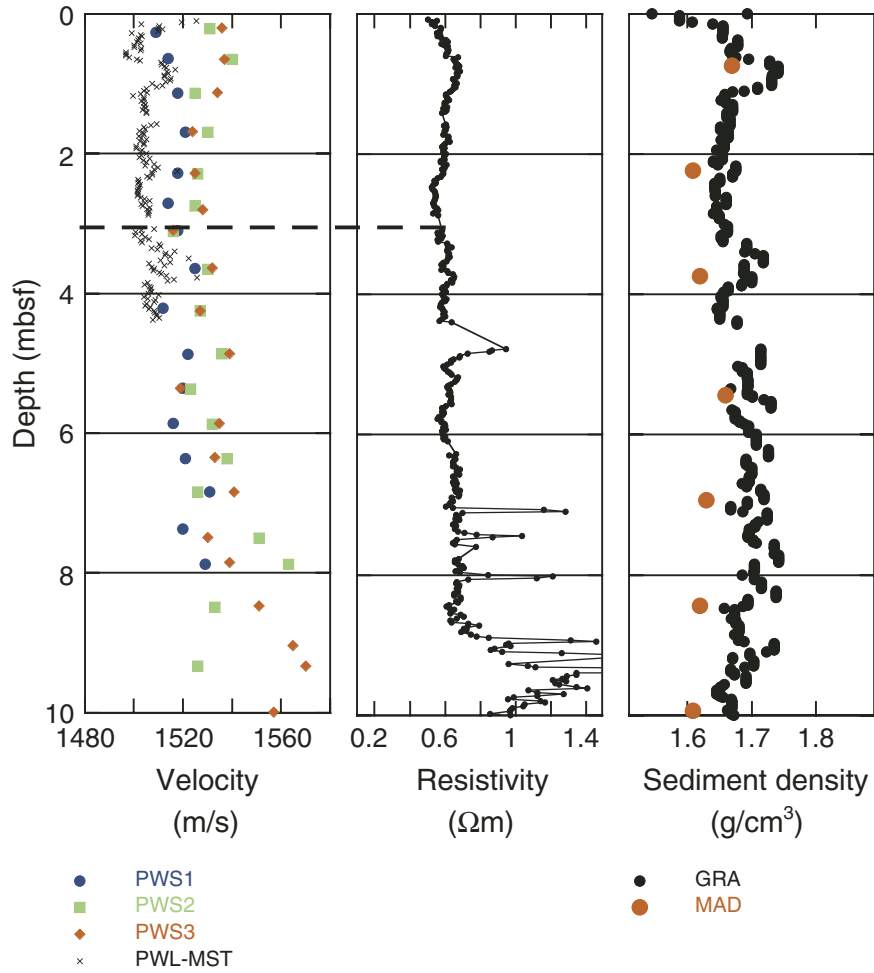


Figure F25. Raw APCT tool data for estimating in situ temperatures. Only the portion of data immediately before, during, and immediately after penetration of the probe into the subsurface is shown. For an example of the entire temperature history of a deployment, see “[Downhole Tools and Pressure Coring](#),” p. 34, in the “Explanatory Notes” chapter. The ODP core identification number associated with each run of the APCT tool is indicated in the upper left corner of the graph. The measurement depth, mudline temperature, extrapolated in situ temperature estimate, and measured thermal conductivity used for the extrapolation are also shown.

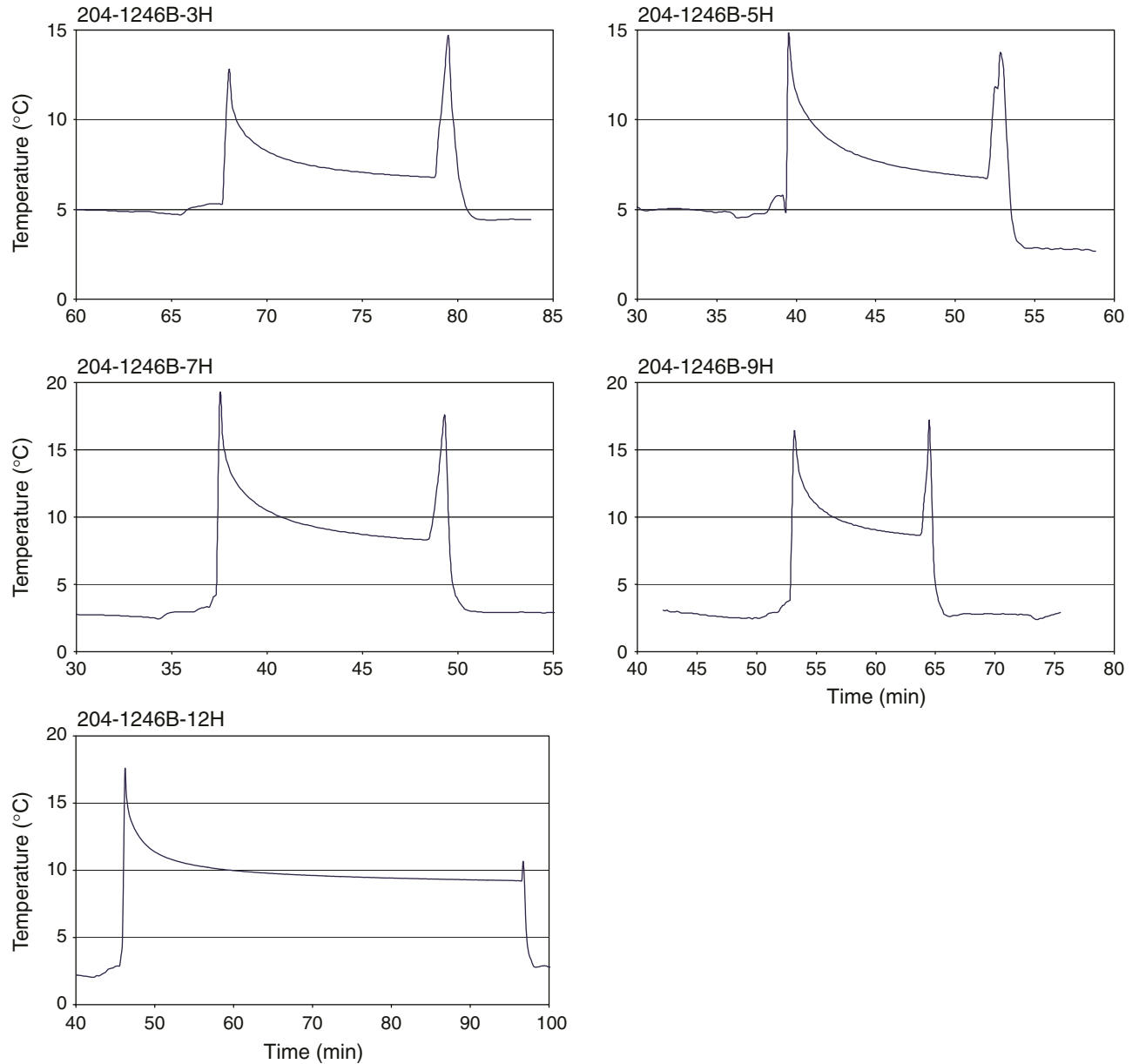


Figure F26. Subsurface temperatures plotted vs. depth beneath the seafloor at Site 1246. The equation for the best fitting linear thermal gradient is shown (dashed line). The gradient determined after correcting the data for an inferred calibration “jump” is also shown (solid line).

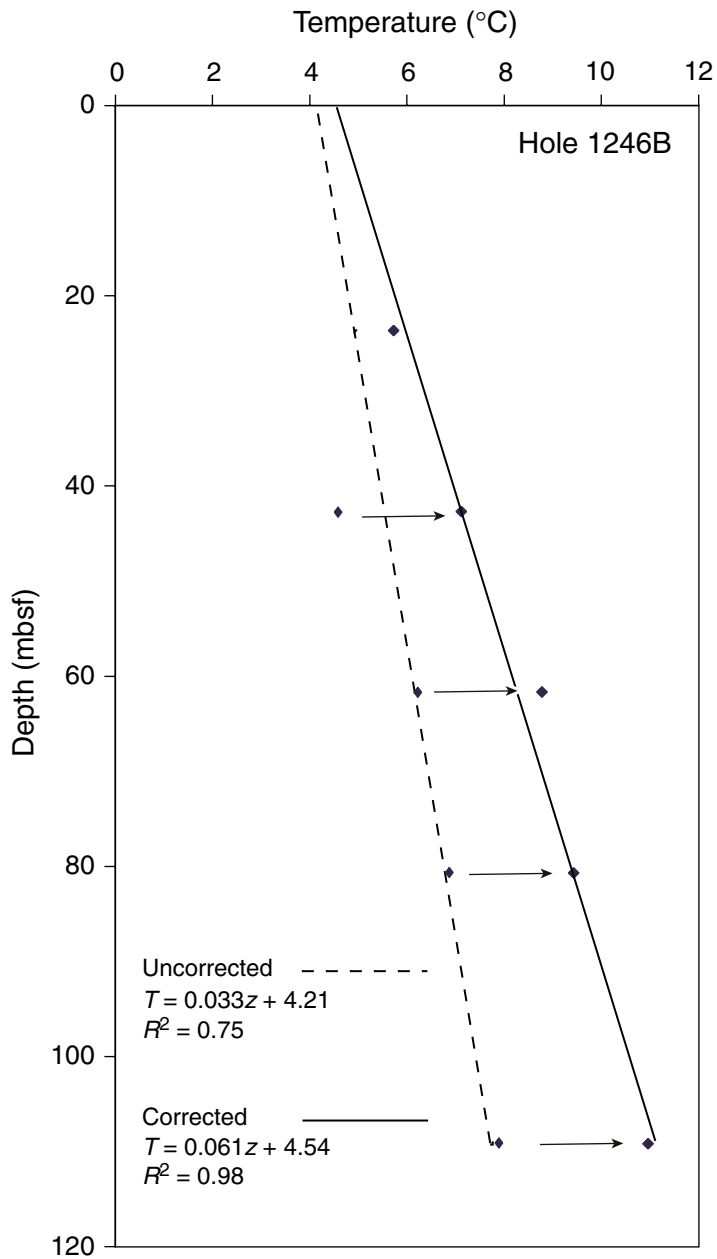


Figure F27. Temperatures recorded during the ice bath advanced piston corer temperature (APCT) tool calibration experiment.

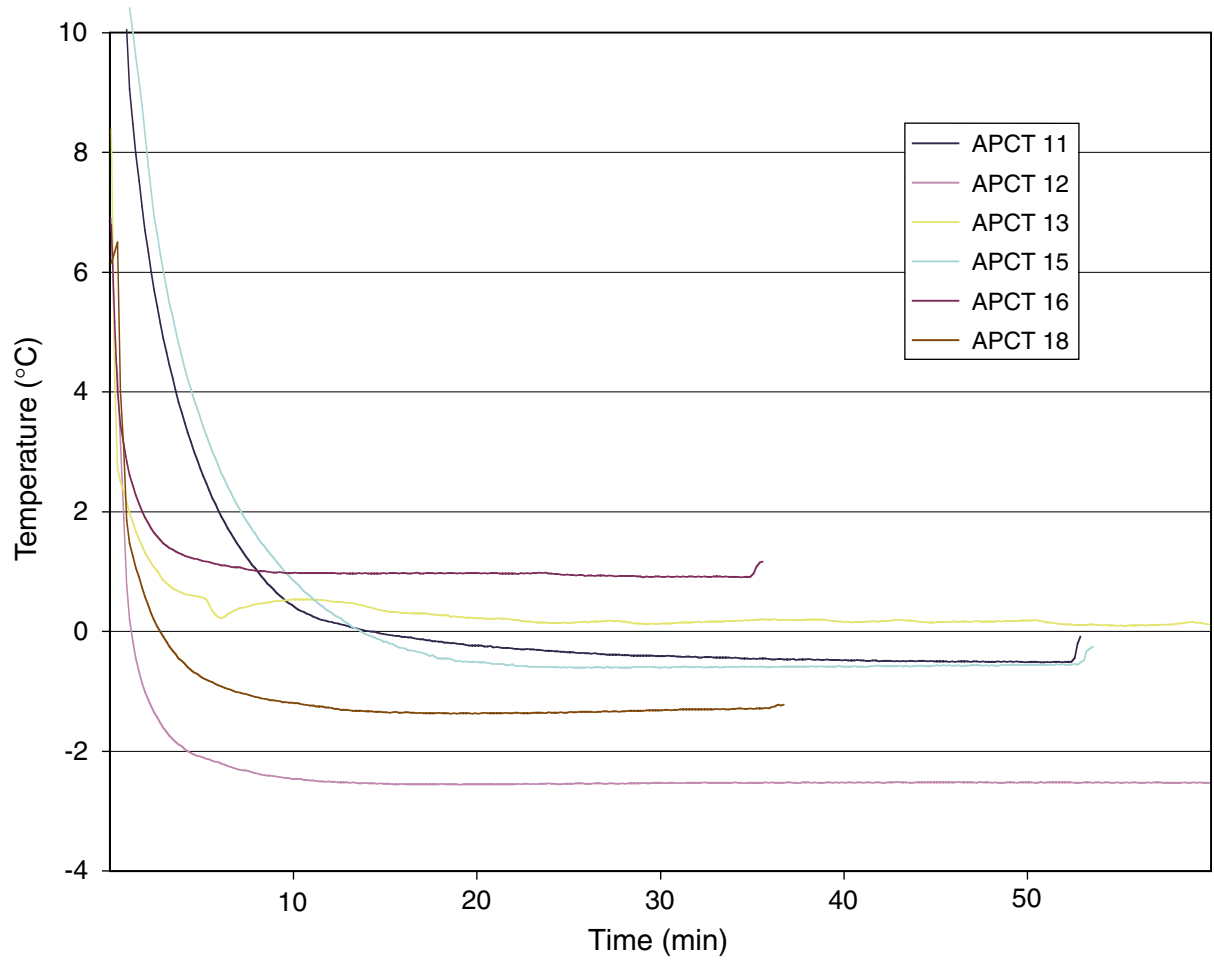


Figure F28. Quality control LWD logs from Hole 1246A. ROP = rate of penetration, TAB = time after bit, Diff. = differential.

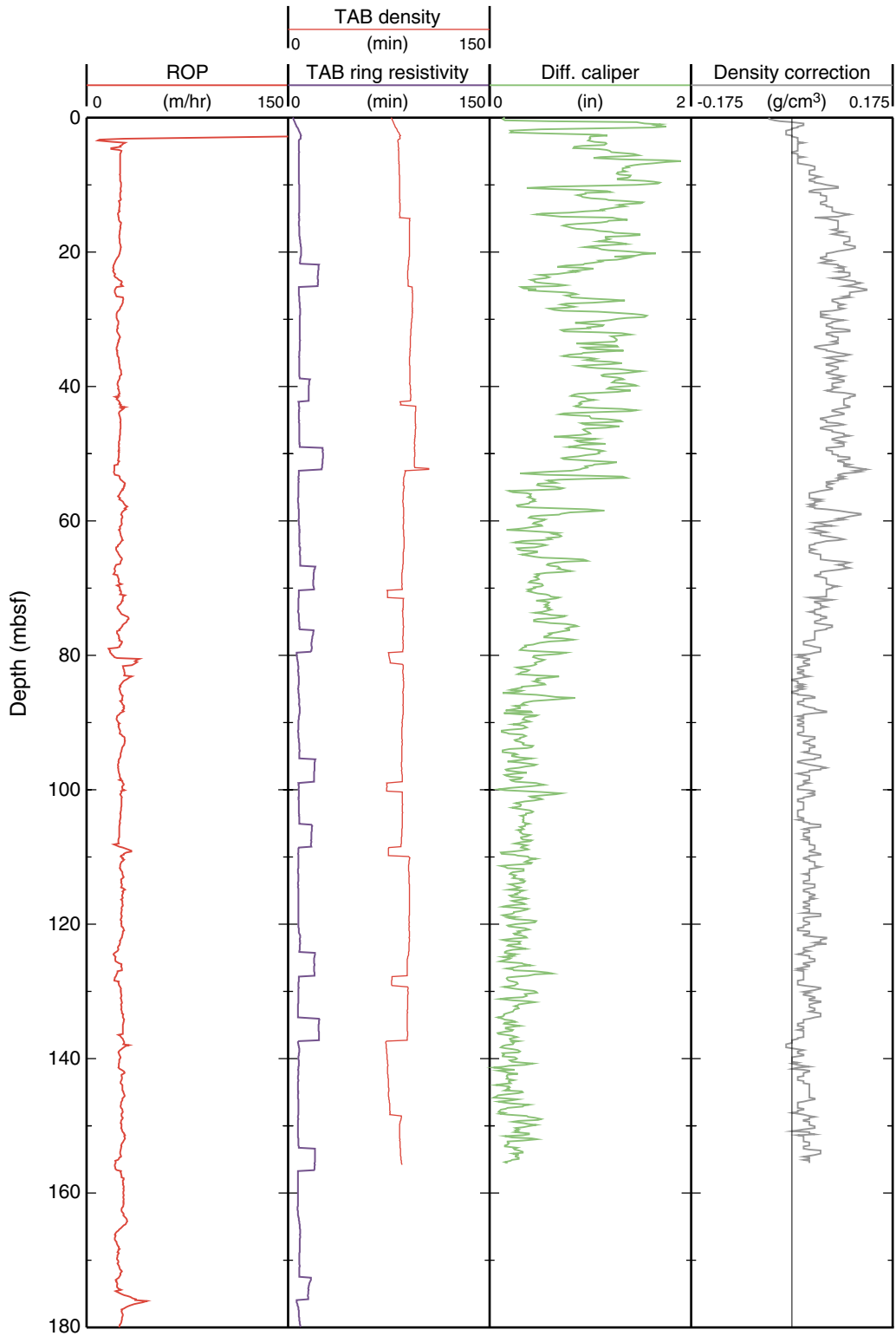


Figure F29. Summary of LWD data from Hole 1246A. gAPI = American Petroleum Institute gamma ray units, PEF = photoelectric effect factor, RAB = resistivity at the bit.

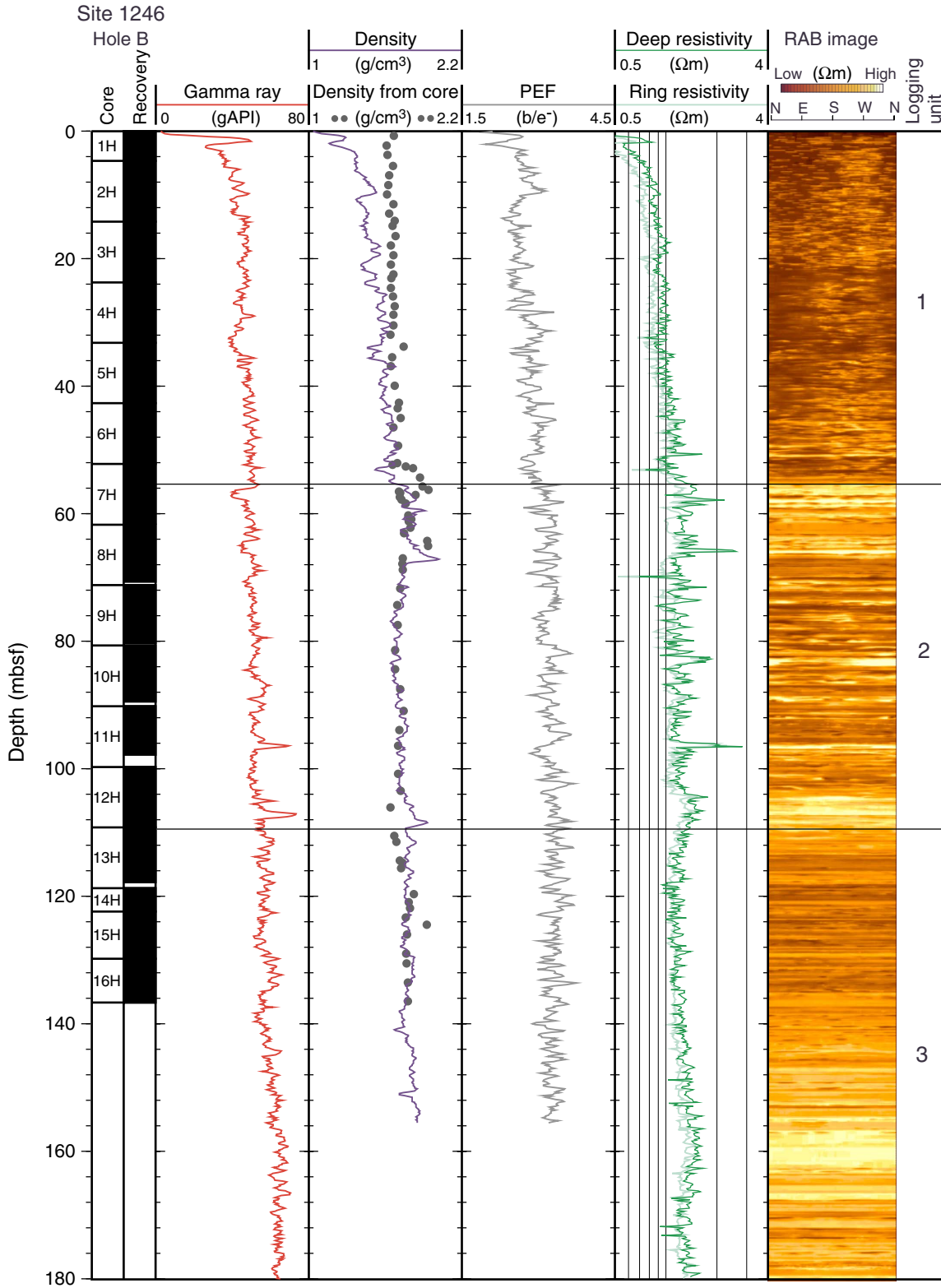


Figure F30. LWD- and core-derived porosities from Hole 1246A. NMR-MRP = Nuclear Magnetic Resonance tool, RAB = resistivity at the bit.

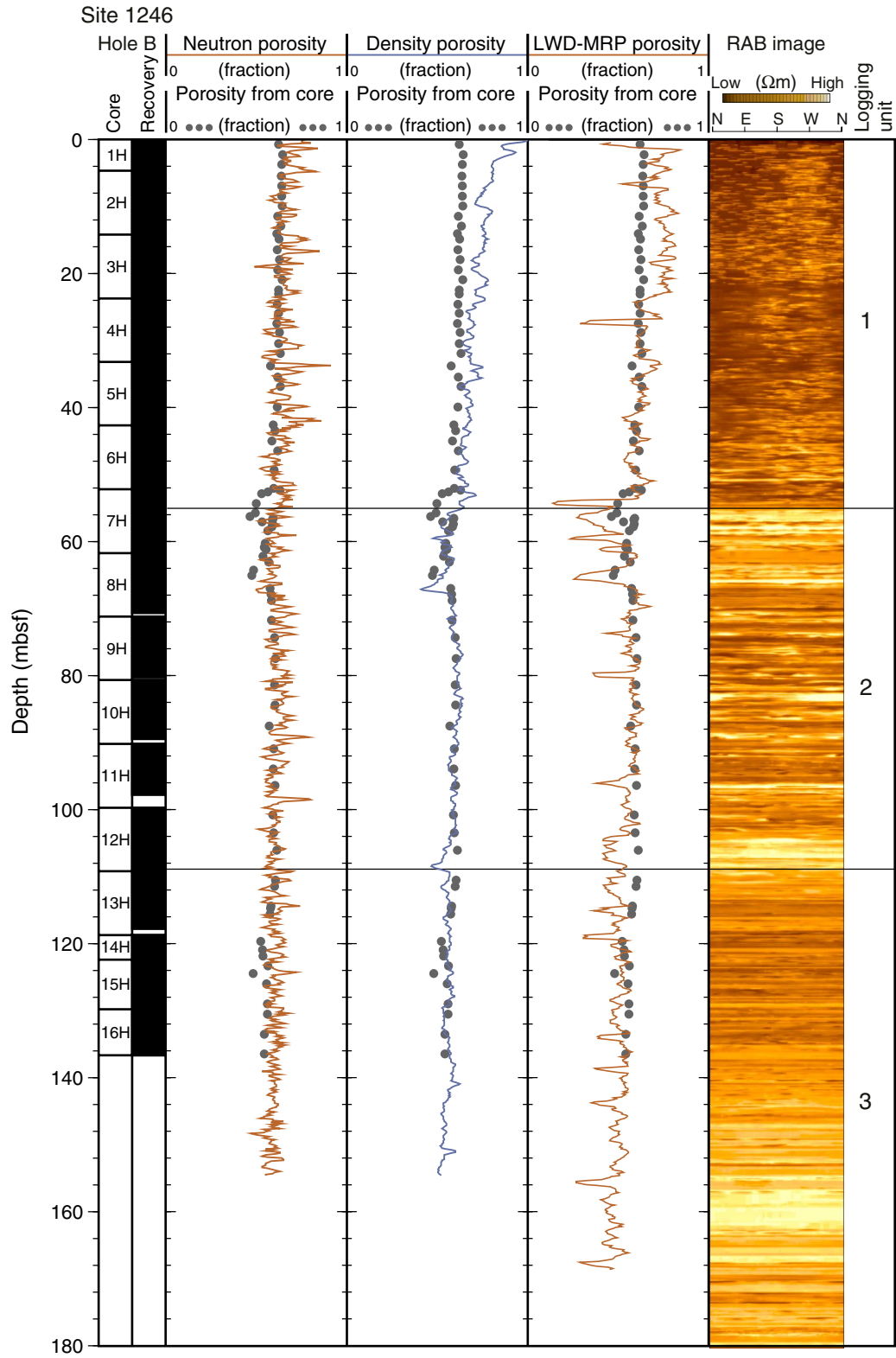


Figure F31. Logging-derived gas hydrate saturations from Hole 1246B. gAPI = American Petroleum Institute gamma ray units, RAB = resistivity at the bit.

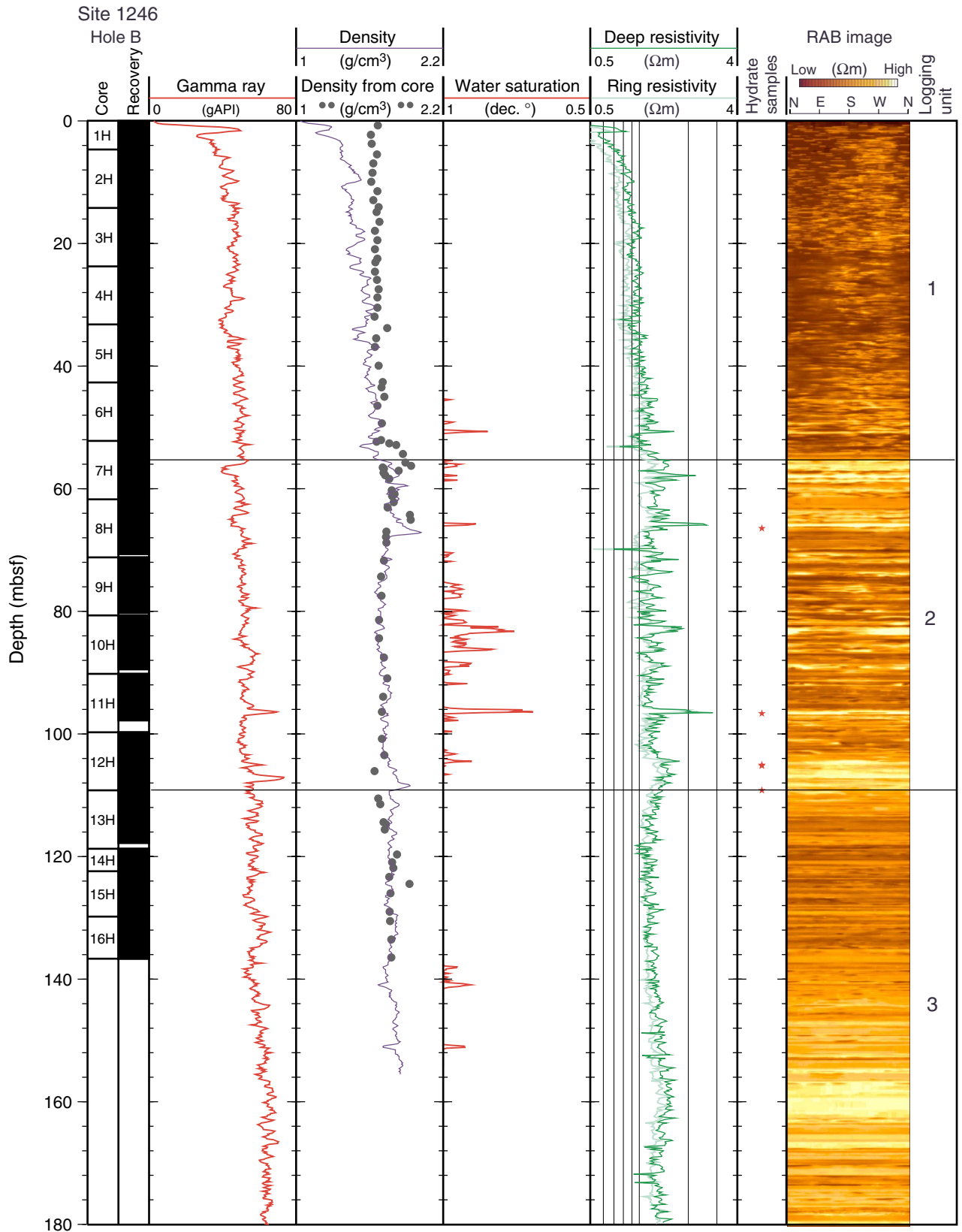


Table T1. Coring summary, Site 1246.

Hole 1246A

Latitude: 44°35.1642'N
 Longitude: 125°8.14'W
 Time on site (hr): 37 (2345 hr, 18 Jul–1800 hr, 19 Jul 2002)
 Time on hole (hr): 18.25 (2345 hr, 18 Jul–1800 hr, 19 Jul 2002)
 Seafloor (drill pipe measurement from rig floor, mbrf): 861.5
 Distance between rig floor and sea level (m): 10.9
 Water depth (drill pipe measurement from sea level, m): 850.6
 Total depth (drill pipe measurement from rig floor, mbrf): 1041.5
 Total penetration (meters below seafloor, mbsf): 180
 Total number of cores: 0
 Total number of drilled intervals: 1
 Total length of cored section (m): 0
 Total core recovered (m): 0
 Core recovery (%): 0

Hole 1246B

Latitude: 44°35.1644'N
 Longitude: 125°8.1235'W
 Time on hole (hr): 18.75 (0400 hr, 11 Aug–2245 hr, 11 Aug 2002)
 Seafloor (drill pipe measurement from rig floor, mbrf): 860.8
 Distance between rig floor and sea level (m): 11.4
 Water depth (drill pipe measurement from sea level, m): 849.4
 Total depth (drill pipe measurement from rig floor, mbrf): 997.5
 Total penetration (meters below seafloor, mbsf): 136.7
 Total number of cores: 16
 Total number of drilled intervals: 0
 Total length of cored section (m): 136.7
 Total core recovered (m): 135.34
 Core recovery (%): 99

Core	Date (Aug 2002)	Local time (hr)	Depth (mbsf)		Length (m)		Recovery (%)
			Top	Bottom	Cored	Recovered	
204-1246A-							
*****Drilled from 0 to 180 mbsf*****							
204-1246B-							
1H	11	0705	0.0	4.7	4.7	4.74	100.9
2H	11	0800	4.7	14.2	9.5	9.78	102.9
3H	11	0900	14.2	23.7	9.5	9.80	103.2
4H	11	0930	23.7	33.2	9.5	10.18	107.2
5H	11	1035	33.2	42.7	9.5	10.07	106.0
6H	11	1100	42.7	52.2	9.5	9.87	103.9
7H	11	1150	52.2	61.7	9.5	9.45	99.5
8H	11	1230	61.7	71.2	9.5	9.00	94.7
9H	11	1335	71.2	80.7	9.5	9.07	95.5
10H	11	1410	80.7	90.2	9.5	8.76	92.2
11H	11	1450	90.2	99.7	9.5	7.63	80.3
12H	11	1625	99.7	109.2	9.5	10.03	105.6
13H	11	1655	109.2	118.7	9.5	8.65	91.1
14H	11	1730	118.7	122.4	3.7	3.92	105.9
15H	11	1830	122.4	129.8	7.4	7.43	100.4
16H	11	2040	129.8	136.7	6.9	6.96	100.9
Cored totals:					136.7	135.34	99.0
Drilled total:					0.0		
Total:					136.7		

Table T2. Bioevents, Hole 1246B.

Age (Ma)	Bioevent	Top		Bottom		Average depth (mbsf)	Event number*	Comment
		Core, section	Depth (mbsf)	Core, section	Depth (mbsf)			
0.30	LO <i>Proboscia curvirostris</i>	204-1246B-4H-CC	33.87	204-1246B-5X-CC	43.22	38.55	1	Diatom
0.27	FO <i>Emiliana huxleyi</i>	9H-CC	80.22	10H-CC	89.41	84.82	2	Nannofossil
0.46	LO <i>Pseudoemiliana lacunosa</i>	11H-CC	96.97	12H-CC	109.70	103.34	3	Nannofossil

Note: * = number in Figure F7, p. 27. FO = first occurrence, LO = last occurrence.

Table T3. Interstitial water data, Hole 1246B.

Core, section, interval (cm)	Depth (mbsf)	pH	Alkalinity (mM)	Salinity (g/kg)	Cl (mM)	SO ₄ (mM)	NH ₄ (mM)	PO ₄ (μM)	Na (mM)	K (mM)	Mg (mM)	Ca (mM)	B (μM)	Ba (μM)	Fe (μM)	Li (μM)	Mn (μM)	Sr (μM)	DOC (mM)
204-1246B-																			
1H-2, 145-150	2.95	—	—	—	545	26.1	0.3	10	488	11.6	39.1	5.08	—	—	—	—	BDL	—	—
2H-2, 145-160	7.65	7.78	32.90	34	556	1.6	2.8	121	488	12.0	37.8	4.31	672	19.8	5.2	12.9	BDL	75.5	4.89
2H-5, 145-150	12.15	7.68	35.68	33	559	1.0	5.3	255	501	11.4	36.1	3.91	724	55.7	6.9	11.7	BDL	83.8	—
3H-2, 140-150	17.10	7.54	38.30	34	552	0.8	7.7	326	496	11.7	33.5	2.67	844	61.7	18.0	13.3	BDL	82.9	10.80
3H-5, 140-150	21.60	7.61	38.18	34	555	1.0	9.2	186	512	12.6	35.1	2.70	790	64.7	3.5	17.9	BDL	79.5	—
4H-2, 140-150	26.60	7.37	40.37	34	552	1.1	10.1	261	507	11.3	35.3	2.54	837	64.8	24.0	20.2	BDL	83.4	12.79
4H-5, 140-150	31.10	7.40	41.16	34	555	1.0	10.9	314	512	11.2	33.4	2.40	798	63.1	20.4	21.3	BDL	86.3	—
5H-2, 140-150	36.10	7.34	42.06	34	551	1.1	12.1	335	516	11.3	32.2	2.44	805	59.2	17.3	22.1	BDL	87.2	13.96
5H-5, 140-150	40.60	7.37	43.66	34	540	1.1	12.5	357	514	11.3	29.1	1.92	877	53.1	31.3	20.2	BDL	81.1	—
6H-2, 140-150	45.57	7.86	42.68	34	552	1.1	14.4	319	523	13.3	31.5	2.28	—	42.0	3.0	19.2	BDL	72.5	17.46
6H-5, 140-150	50.00	7.49	46.80	34	554	0.7	14.2	329	523	11.6	32.1	2.51	840	47.2	5.9	19.0	BDL	88.8	—
7H-2, 140-150	54.99	7.55	49.13	34	555	0.9	15.4	327	524	12.1	30.8	2.42	819	40.4	4.6	14.7	BDL	87.5	15.70
7H-5, 140-150	59.49	7.90	52.26	34	557	0.5	17.0	318	481	13.5	31.2	2.48	719	44.9	2.0	14.4	BDL	85.4	—
8H-2, 140-150	64.60	7.63	55.57	35	556	0.6	17.0	334	486	12.6	22.3	1.86	755	47.2	3.1	15.1	BDL	85.8	16.19
8H-4, 0-25	66.20	7.99	46.03	28	433	1.4	15.2	156	381	11.4	32.2	2.69	—	27.4	1.5	12.2	BDL	52.5	—
8H-5, 140-150	69.10	7.59	58.61	35	560	0.9	18.6	189	487	13.0	32.6	2.74	830	50.1	1.8	18.2	BDL	81.2	17.48
9H-2, 140-150	73.81	7.66	63.76	35	558	1.3	19.6	273	485	12.6	31.4	2.48	850	56.2	6.5	21.7	BDL	79.8	13.63
9H-5, 140-150	78.31	7.85	61.66	34	523	1.1	18.6	284	463	12.3	31.0	3.09	752	52.4	6.7	21.4	BDL	67.5	—
9H-7, 52-68	79.93	7.43	45.55	32	497	6.4	16.0	311	428	10.8	32.6	2.73	745	27.4	5.3	20.9	BDL	67.5	—
10H-2, 140-150	83.60	7.51	63.12	35	542	1.3	19.0	329	476	12.1	33.4	2.87	858	58.6	4.2	26.6	BDL	79.3	18.01
10H-5, 132-142	88.02	7.70	67.54	35	553	1.9	20.6	244	479	13.5	35.9	2.91	813	69.2	3.8	31.6	BDL	87.2	—
11H-2, 140-150	93.10	7.47	70.63	36	554	1.1	20.0	393	491	12.3	33.3	2.94	863	72.2	7.8	31.8	BDL	87.9	18.56
11H-5, 83-93	96.54	7.82	67.99	35	554	1.2	21.4	290	484	13.8	35.2	2.61	761	56.8	6.6	32.6	BDL	72.4	—
12H-2, 140-150	102.60	7.78	71.08	36	553	0.0	21.7	333	487	13.2	32.4	2.69	729	65.7	4.9	33.5	BDL	83.4	19.53
12H-4, 67-87	104.73	7.36	66.19	32	495	1.7	19.6	394	429	10.9	33.8	3.12	799	63.2	4.0	28.6	BDL	81.8	—
12H-5, 0-20	105.33	7.50	69.76	34	534	2.2	20.9	361	464	11.8	36.2	4.38	690	73.8	3.6	30.2	BDL	86.4	19.62
12H-5, 20-36	105.53	7.47	74.85	36	553	1.2	21.1	400	483	12.3	37.3	3.04	852	81.9	7.0	34.4	BDL	98.3	—
13H-2, 135-150	112.05	7.54	77.90	36	553	1.0	22.2	331	482	12.8	40.6	3.30	758	85.8	4.3	36.6	BDL	94.7	—
13H-5, 135-150	116.55	7.94	78.35	36	552	0.5	20.7	214	479	13.4	43.7	5.20	734	85.7	6.5	37.6	BDL	89.5	18.95
14H-2, 135-150	121.55	7.51	80.76	36	554	1.1	21.8	243	481	12.6	42.6	4.20	722	125.7	7.9	39.7	BDL	103.0	19.95
15H-2, 140-150	125.15	7.50	79.00	36	551	0.9	23.2	188	464	12.6	43.5	5.60	753	136.7	5.4	44.3	BDL	103.4	19.98
15H-4, 140-150	128.15	7.29	83.14	36	553	0.7	22.1	330	471	11.8	43.8	5.00	863	167.6	10.3	45.8	BDL	110.7	19.09
16H-2, 140-150	132.70	7.27	81.42	36	550	1.2	22.7	240	468	12.0	—	—	845	186.9	14.8	48.7	BDL	112.7	17.44

Notes: DOC = dissolved organic carbon. — = no sample was available. BDL = below detection limits.

Table T4. Concentrations of methane, ethane, ethylene, and propane in headspace gas, Hole 1246B.

Core, section, interval (cm)	Depth (mbsf)	C ₁ (ppmv)	C ₂ (ppmv)	C ₂₌ (ppmv)	C ₃ (ppmv)	C ₁ /C ₂	C ₁ (mM)
204-1246B-							
1H-1, 0-5	0.00	18					0.004
1H-2, 0-5	1.50	8					0.002
1H-3, 0-5	3.00	3					0.001
2H-3, 0-5	7.70	4,879	1.2	0.6		4,135	0.8
2H-6, 0-5	12.20	60,636	1.7	0.8		36,749	8.2
3H-3, 0-5	17.20	24,914	1.2	0.5		20,936	3.7
3H-6, 0-5	21.70	17,611	1.3	0.6		13,977	2.5
4H-3, 0-5	26.70	15,711	1.0			15,403	2.6
4H-6, 0-5	31.20	29,532	1.4	0.6		20,945	4.0
5H-3, 0-5	36.20	13,865	1.1			13,080	2.5
5H-6, 0-5	40.70	16,757	1.0			17,099	2.9
6H-3, 0-5	45.67	25,858	1.3			20,361	4.2
6H-6, 0-5	50.10	17,368	0.6			29,437	2.7
7H-3, 0-5	55.09	12,921					2.5
7H-6, 0-5	59.59	13,624					2.6
8H-3, 0-5	64.70	9,877		0.4			1.6
8H-6, 0-5	69.20	10,887					2.2
9H-3, 0-5	73.91	13,192	0.5	0.6		24,430	2.7
9H-6, 0-5	78.41	12,499	0.5	0.7		24,998	2.7
10H-3, 0-5	83.70	21,638	1.6	0.4		13,609	4.1
10H-6, 0-5	88.12	11,259	0.4			31,275	2.5
11H-3, 0-5	93.20	15,995	0.7	0.7		22,528	3.5
11H-5, 0-5	95.71	14,398	0.7	0.7		20,569	2.9
12H-3, 0-5	102.70	10,436	0.7			16,055	2.2
12H-6, 0-5	106.83	22,934	3.8			6,019	4.1
13H-3, 0-5	112.20	17,540	9.4	0.3	12.8	1,864	4.0
14H-3, 0-5	121.70	11,805	24.6		22.2	480	2.7
15X-4, 0-5	126.75	22,287	50.2	0.5	29.7	444	3.7
16X-3, 0-5	132.80	13,269	40.2		24.7	330	3.4
16X-5, 0-5	135.80	24,932	65.5	0.6	40.1	381	4.9

Note: C₁ = methane, C₂ = ethane, C₂₌ = ethylene, C₃ = propane.

Table T5. Concentrations of light hydrocarbon and nonhydrocarbon gases in VAC samples of core gas void, Hole 1246B.

Core, section, interval (cm)	Depth (mbsf)	C ₁ (ppmv)	C ₂ (ppmv)	C ₃ (ppmv)	<i>i</i> -C ₄ (ppmv)	<i>n</i> -C ₄ (ppmv)	<i>i</i> -C ₅ (ppmv)	<i>n</i> -C ₅ (ppmv)	CO ₂ (ppmv)	O ₂ (ppmv)	N ₂ (ppmv)	C ₁ /C ₂	
204-1246B-													
3H-3, 20	17.40	926,788	8.5						7,353	8,670	35,729	109,034	
4H-1, 97	24.67	935,966	9.0	6.7					13,845	5,510	22,577	104,344	
5H-3, 62	36.82	936,565	12.5						13,393	5,459	21,845	75,166	
6H-4, 71	47.81	964,256	18.3						3,409	2,120	3,588	52,807	
7H-3, 1	55.10	959,957	13.0						7,750	1,117	1,530	73,843	
8H-4, 5	66.25	969,246	21.7						2,553	675	931	44,584	
9H-2, 1	72.42	957,787	15.5									61,713	
10H-1, 100	81.70	962,084	17.1									56,361	
11H-2, 33	92.03	958,690	10.3									93,531	
12H-2, 100	102.20	956,954	37.1						9,345	1,132	1,074	25,801	
13H-1, 149	110.69	960,526	357.1						9,637	991	949	2,690	
14H-2, 102	121.22	946,392	399.2	150.9					18,688	1,312	1,161	2,371	
15H-2, 0	123.75	952,490	493.4	181.8	27.4				12,808	1,842	2,067	1,930	
15H-5, 24	128.49	949,495	539.0	213.0	37.8				8.7	17,463	1,551	1,584	1,762
16H-4, 73	135.03	953,243	636.0	185.6	28.3					16,124	771	1,165	1,499

Note: C₁ = methane, C₂ = ethane, C₃ = propane, *i*-C₄ = iso-butane, *n*-C₄ = normal butane, *i*-C₅ = iso-pentane, *n*-C₅ = normal pentane, CO₂ = carbon dioxide, O₂ = oxygen, N₂ = nitrogen.

Table T6. Composition of gas from analyses of decomposed samples of gas hydrate, Hole 1246B.

Core, section, interval (cm)	Depth (mbsf)	C ₁ (ppmv)	C ₂ (ppmv)	C ₃ (ppmv)	<i>i</i> -C ₄ (ppmv)	<i>n</i> -C ₄ (ppmv)	H ₂ S (ppmv)	CO ₂ (ppmv)	O ₂ (ppmv)	N ₂ (ppmv)	C ₁ /C ₂
204-1246B-12H-4, 87	104.93	919,966	17.1	8.3				4,505	11,324	36,719	53,957

Note: C₁ = methane, C₂ = ethane, C₃ = propane, *i*-C₄ = iso-butane, *n*-C₄ = normal butane, H₂S = hydrogen sulfide, CO₂ = carbon dioxide, O₂ = oxygen, N₂ = nitrogen.

Table T7. Carbonate carbon, calcium carbonate, total carbon, organic carbon, total nitrogen, and total sulfur contents and C/N ratios, Hole 1246B.

Core, section, interval (cm)	Depth (mbsf)	Carbonate carbon (wt%)	CaCO ₃ (wt%)	Total carbon (wt%)	Organic carbon (wt%)	Total nitrogen (wt%)	Total sulfur (wt%)	C/N
204-1246B-								
1H-3, 74-76	3.74	0.14	1.14	1.73	1.59	0.15	0.89	10.6
2H-3, 75-76	8.45	0.16	1.35	1.21	1.05	0.12	1.02	8.75
3H-3, 75-76	17.95	0.39	3.26	1.85	1.46	0.17	0.58	8.59
4H-3, 75-76	27.45	0.77	6.42	2.02	1.25	0.17	0.17	7.35
5H-3, 68-69	36.88	0.74	6.17	1.69	0.95	0.15	0.11	6.33
6H-3, 79-80	46.46	0.35	2.92	1.37	1.02	0.16	0.26	6.38
7H-3, 130-131	56.39	0.32	2.67	0.69	0.37	0.06	0.09	6.17
8H-4, 87-88	67.07	0.33	2.72	1.24	0.91	0.17	0.11	5.35
9H-3, 47-48	74.38	0.30	2.54	1.62	1.32	0.18	0.21	7.33
10H-3, 72-73	84.42	0.50	4.19	1.97	1.47	0.20	0.35	7.35
11H-3, 76-77	93.96	0.39	3.27	1.74	1.35	0.19	0.31	7.11
12H-3, 76-77	103.46	0.60	5.00	1.69	1.09	0.18	0.14	6.06
13H-4, 72-73	114.42	0.81	6.75	1.96	1.15	0.17	1.25	6.76
14H-3, 14-15	121.84	0.15	1.22	1.43	1.28	0.19	0.48	6.74
15H-3, 75-76	126.00	0.34	2.83	1.64	1.30	0.20	0.31	6.50
16H-3, 75-76	133.55	0.16	1.35	1.84	1.68	0.19	0.48	8.84

Note: CaCO₃ = calcium carbonate.

Table T8. Rock-Eval pyrolysis of samples, Hole 1246B.

Core, section, interval (cm)	Depth (mbsf)	Organic carbon (wt%)	S ₁ (mg/g)	S ₂ (mg/g)	Production index (S ₁ /[S ₁ +S ₂])	Hydrogen index (mg S ₂ /g C)	T _{max} (°C)
204-1246B-							
1H-3, 74-76	3.74	1.73	0.02	0.18	0.10	10	407
4H-3, 75-76	27.45	2.02	0.41	1.90	0.18	94	412
9H-3, 47-48	74.38	1.62	0.37	2.13	0.15	131	
10H-3, 72-73	84.42	1.97	0.38	2.37	0.14	120	412
12H-3, 75-76	103.46	1.68	0.27	1.24	0.18	74	410
14H-3, 14-15	121.84	1.43	0.32	1.90	0.14	133	467
16H-3, 75-76	133.55	1.68	0.40	2.88	0.12	171	412

Notes: NA = not analyzed. S₁ and S₂ are as defined in **“Organic Matter Characterization,”** p. 18, in **“Organic Geochemistry”** in the **“Explanatory Notes”** chapter.

Table T9. Presence of gas hydrate based on infrared images of cores in liners, Hole 1246B.

Core, section	ΔT (°C)	Gas hydrate texture	Depth interval (mbsf)*		Anomaly designation†	Hydrate sample		
			Top	Bottom		Top (cm)	Bottom (cm)	Depth (mbsf)
204-1246B-								
3H	-0.5	Disseminated; subtle but real anomaly	16.00	17.40	IR164			
3H	-1.8	Disseminated; subtle but real anomaly	18.00	19.00	IR165			
3H	-1.4	Disseminated; subtle but real anomaly	19.70	21.90	IR166			
4H	-0.3	Disseminated; subtle but real anomaly	25.00	29.40	IR167			
4H	-0.4	Disseminated; subtle but real anomaly	31.40	32.60	IR168			
5H	-0.3	Disseminated; distinct on image	34.50	35.00	IR169			
5H	-0.7	Disseminated; but sharp on plot	36.00	36.10	IR170			
5H	-1.8	Disseminated; first sharp single anomaly	38.10	38.40	IR171			
5H	-1.0	Disseminated; largest ΔT at center	40.00	41.00	IR172			
5H	-0.7	Disseminated; some suggestion of layering	42.20	42.30	IR173			
6H	-0.6	Disseminated	43.40	43.50	IR174			
6H	-0.9	Disseminated; void in middle	44.60	44.80	IR175			
6H	-0.5	Disseminated	46.20	46.40	IR176			
6H	-1.2	Disseminated	49.70	49.80	IR177			
6H	-1.3	Vein; moderate dip	51.00	51.50	IR178			
6H	-0.6	Disseminated	53.10	53.30	IR179			
7H	-1.5	Disseminated; horizontal layering; disrupted at top (?)	56.80	57.30	IR180			
7H	-0.6	Disseminated; layer	59.35	59.45	IR181			
7H	-1.4	Disseminated	61.50	61.60	IR182			
8H	-0.3	Disseminated	61.80	61.90	IR183			
8H	-0.7	Disseminated	63.00	63.40	IR184			
8H-4	-4.0	Stratigraphically controlled hydrate	66.00	66.50	IR185	25	30	66.45
8H	-1.0	Disseminated	66.75	67.10	IR186			
8H	-1.4	Disseminated	67.20	67.40	IR187			
9H	-0.7	Disseminated	71.40	71.80	IR188			
9H	-0.6	Disseminated	72.10	72.40	IR189			
9H	-2.1	Disseminated	72.80	73.30	IR190			
9H	-0.4	Disseminated	74.90	75.00	IR191			
9H	-0.4	Disseminated	75.90	76.00	IR192			
9H	-1.8	Disseminated; vein	76.10	77.00	IR193			
9H	-0.9	Disseminated; nodular	78.20	79.10	IR194			
9H	-2.0	Vein; nodular	80.10	81.20	IR195			
10H	-1.2	Disseminated	81.80	81.90	IR196			
10H	-0.8	Disseminated	82.10	82.30	IR197			
10H	-1.5	Vein	84.30	84.50	IR198			
10H	-3.0	Nodular; possible. dipping rod shape	85.70	86.00	IR199			
10H	-1.0	Nodular	86.10	86.20	IR202			
10H	-2.5	Vein; parallel to bedding	88.00	88.20	IR200			
10H	-1.5	Disseminated	89.00	89.20	IR201			
11H	-1.1	Disseminated	90.30	90.70	IR203			
11H	-1.0	Disseminated	92.70	92.90	IR204			
11H	-0.6	Disseminated	93.90	94.00	IR205			
11H-5	-4.4	Vein	96.80	97.10	IR206	93	126	96.64
12H-4	-1.6	Disseminated	99.70	100.00	IR207			
12H	-6.6	Nodular on steeply dipping plane	104.80	105.30	IR208	102	127	105.08
12H	-1.8	Disseminated	106.10	106.50	IR209			
12H	-0.6	Disseminated	107.70	107.80	IR210			
13H-1	-3.1	Nodular	109.20	109.70	IR211	0	30	109.20
13H	-0.8	Disseminated	109.80	110.40	IR212			
13H	-0.8	Disseminated	111.00	111.20	IR213			
13H	-0.7	Disseminated	114.20	114.30	IR214			
13H	-0.8	Disseminated	115.00	115.10	IR215			
13H	-0.6	Disseminated	115.60	115.70	IR216			
13H	-0.5	Disseminated	116.70	116.80	IR217			
Additional sample								
12H-4						87	102	104.93

Notes: * = from uncut core liner. † = designation used for reference to specific anomalies in text and figures. Difference between these depth intervals and the equivalent curated section depth intervals is typically <1 m.

Table T10. Moisture and density, Hole 1246B.

Core, section, interval (cm)	Depth (mbsf)	Density (g/cm ³)		Porosity (%)	Core, section, interval (cm)	Depth (mbsf)	Density (g/cm ³)		Porosity (%)
		Bulk	Grain				Bulk	Grain	
204-1246B-					7H-4, 48-50	57.07	1.837	2.758	53.1
1H-1, 74-76	0.74	1.668	2.733	62.3	7H-4, 80-82	57.39	1.712	2.704	59.0
1H-2, 74-76	2.24	1.609	2.675	64.5	7H-4, 118-120	57.77	1.727	2.716	58.4
1H-3, 74-76	3.74	1.616	2.664	63.9	7H-5, 34-36	58.43	1.761	2.705	56.2
2H-1, 74-76	5.44	1.660	2.779	63.7	7H-6, 70-72	60.29	1.779	2.698	54.9
2H-2, 74-76	6.94	1.630	2.707	64.0	7H-7, 28-30	60.87	1.803	2.732	54.4
2H-3, 74-76	8.44	1.622	2.678	63.9	7H-7, 60-62	61.19	1.782	2.716	55.2
2H-4, 74-76	9.94	1.612	2.664	64.2	8H-1, 48-50	62.18	1.798	2.687	53.5
2H-5, 74-76	11.44	1.663	2.693	61.7	8H-1, 140-142	63.10	1.746	2.698	56.8
2H-6, 74-76	12.94	1.631	2.685	63.5	8H-2, 110-112	64.30	1.929	2.782	48.5
2H-7, 38-40	14.08	1.674	2.705	61.3	8H-3, 38-40	65.08	1.938	2.764	47.5
3H-1, 66-68	14.86	1.658	2.714	62.5	8H-4, 82-84	67.02	1.737	2.701	57.5
3H-2, 74-76	16.44	1.679	2.718	61.4	8H-5, 16-18	67.86	1.732	2.709	58.0
3H-3, 74-76	17.94	1.643	2.681	62.6	8H-5, 112-114	68.82	1.736	2.730	58.3
3H-4, 74-76	19.44	1.665	2.704	61.8	9H-1, 53-55	71.73	1.716	2.684	58.3
3H-5, 74-76	20.94	1.645	2.752	64.1	9H-3, 44-46	74.35	1.692	2.699	60.1
3H-6, 74-76	22.44	1.662	2.713	62.2	9H-5, 58-60	77.49	1.698	2.728	60.4
3H-7, 35-37	23.05	1.646	2.672	62.3	10H-1, 70-72	81.40	1.676	2.653	60.0
4H-1, 89-91	24.59	1.644	2.638	61.6	10H-3, 70-72	84.40	1.678	2.673	60.3
4H-2, 74-76	25.94	1.661	2.709	62.2	10H-5, 86-88	87.56	1.716	2.634	57.0
4H-3, 74-76	27.44	1.673	2.703	61.3	11H-1, 74-76	90.94	1.744	2.798	59.4
4H-4, 63-65	28.83	1.662	2.730	62.6	11H-3, 74-76	93.94	1.709	2.708	59.3
4H-5, 74-76	30.44	1.663	2.718	62.3	11H-5, 72-74	96.43	1.699	2.718	60.2
4H-6, 74-76	31.94	1.641	2.697	63.1	12H-1, 110-112	100.80	1.699	2.668	58.9
5H-1, 63-65	33.83	1.745	2.737	57.9	12H-3, 74-76	103.44	1.720	2.743	59.5
5H-2, 78-80	35.48	1.652	2.665	61.7	12H-5, 74-76	106.07	1.641	2.614	61.2
5H-3, 68-70	36.88	1.644	2.710	63.2	13H-1, 133-135	110.53	1.671	2.658	60.4
5H-5, 74-76	39.94	1.672	2.706	61.5	13H-2, 76-78	111.46	1.686	2.677	60.0
5H-7, 40-42	42.60	1.706	2.700	59.3	13H-4, 72-74	114.42	1.714	2.667	58.0
6H-1, 78-80	43.48	1.698	2.721	60.3	13H-4, 105-107	114.75	1.735	2.706	57.8
6H-2, 81-83	44.98	1.721	2.705	58.5	13H-5, 42-44	115.62	1.723	2.672	57.6
6H-3, 79-81	46.46	1.663	2.698	61.8	14H-1, 94-96	119.64	1.824	2.704	52.4
6H-5, 74-76	49.34	1.701	2.706	59.7	14H-2, 74-76	120.94	1.784	2.655	53.4
6H-7, 48-50	52.08	1.693	2.676	59.5	14H-3, 14-16	121.84	1.795	2.682	53.5
7H-1, 12-14	52.32	1.658	2.738	63.0	15H-1, 95-97	123.35	1.759	2.703	56.2
7H-1, 40-42	52.60	1.761	2.709	56.3	15H-2, 71-73	124.46	1.926	2.762	48.1
7H-1, 64-66	52.84	1.817	2.709	52.9	15H-3, 74-76	125.99	1.769	2.701	55.6
7H-2, 74-76	54.33	1.872	2.720	50.0	15H-5, 74-76	128.99	1.763	2.703	56.0
7H-3, 62-64	55.71	1.892	2.744	49.5	16H-1, 76-78	130.56	1.766	2.713	56.1
7H-3, 118-120	56.27	1.940	2.733	46.4	16H-3, 74-76	133.54	1.776	2.667	54.2
7H-3, 144-146	56.53	1.706	2.697	59.3	16H-5, 65-67	136.45	1.778	2.674	54.3
7H-4, 14-16	56.73	1.716	2.700	58.7					

Table T11. Compressional wave velocity measurements, Hole 1246B.

Core, section, interval (cm)	Depth (mbsf)	PWS3	PWS2	PWS1
204-1246B-				
1H-1, 20.5	0.21	1536		
1H-1, 21.1	0.21		1531	
1H-1, 26.9	0.27			1509
1H-1, 64.3	0.64			1514
1H-1, 64.7	0.65		1540	
1H-1, 65.5	0.66	1537		
1H-1, 113.2	1.13	1534		
1H-1, 113.6	1.14			1518
1H-1, 114.1	1.14		1525	
1H-2, 19.1	1.69	1524		
1H-2, 19.8	1.70			1521
1H-2, 19.8	1.70		1530	
1H-2, 78.5	2.29		1526	
1H-2, 78.5	2.29	1525		
1H-2, 78.8	2.29			1518
1H-2, 121.1	2.71			1514
1H-2, 124.6	2.75		1525	
1H-2, 130.7	2.81	1528		
1H-3, 10.1	3.10	1516		
1H-3, 11.2	3.11			1518
1H-3, 11.5	3.12		1516	
1H-3, 63.5	3.64	1532		
1H-3, 65.1	3.65			1525
1H-3, 65.3	3.65		1530	
1H-3, 121.2	4.21			1512
1H-3, 125.1	4.25		1527	
1H-3, 125.7	4.26	1527		
2H-1, 17.0	4.87		1536	
2H-1, 17.2	4.87			1522
2H-1, 60.3	5.36			1520
2H-1, 66.3	5.37	1519		
2H-1, 67.0	5.37		1523	
2H-1, 116.3	5.86			1516
2H-1, 116.7	5.87	1535		
2H-1, 117.2	5.87		1532	
2H-2, 14.9	6.35	1533		
2H-2, 16.6	6.37			1521
2H-2, 16.7	6.37		1538	
2H-2, 64.6	6.85	1541		
2H-2, 64.7	6.85			1531
2H-2, 64.8	6.88		1526	
2H-2, 117.4	7.37			1520
2H-2, 129.6	7.50	1530		
2H-2, 130.2	7.50		1551	
2H-3, 15.1	7.85	1539		
2H-3, 17.8	7.88			1529
2H-3, 18.0	7.88		1563	
2H-3, 77.6	8.48	1551		
2H-3, 78.8	8.49		1533	
2H-3, 134.4	9.04	1565		
2H-4, 13.1	9.33	1570		
2H-4, 13.3	9.33		1526	
2H-4, 79.8	10.00	1557		

Table T12. Thermal conductivity, Hole 1246B.

Core, section, interval (cm)	Depth (mbsf)	Thermal conductivity (W/[m-K])	Individual measurements (W/[m-K])		
204-1246B-					
1H-2, 75	2.25	1.043	1.062	1.044	1.024
2H-3, 75	8.45	1.033	1.038	1.029	1.033
3H-1, 75	14.95	0.937	0.928	0.946	0.937
3H-3, 75	17.95	0.995	0.983	0.981	1.020
3H-5, 46	20.66	0.925	0.916	0.931	0.927
4H-3, 75	27.45	0.914	0.901	0.940	0.901
5H-1, 100	34.20	0.811	0.812	0.806	0.814
5H-3, 63	36.83	0.835	0.841	0.830	0.835
5H-5, 50	39.70	0.95	0.950	0.954	0.947
6H-3, 35	46.02	0.977	0.965	0.976	0.989
7H-2, 75	54.34	1.042	1.045	1.054	1.026
7H-3, 75	55.84	1.072	1.090	1.068	1.058
7H-5, 75	58.84	0.959	0.971	0.930	0.976
8H-3, 87	65.57	1.067	1.091	1.060	1.049
9H-1, 89	72.09	0.974	0.997	0.969	0.955
9H-4, 65	76.06	0.845	0.840	0.855	0.839
9H-5, 55	77.46	0.921	0.920	0.915	0.929
10H-3, 30	84.00	0.862	0.865	0.863	0.859
11H-3, 110	94.30	0.953	0.946	0.956	0.956
12H-1, 104	100.74	0.924	0.926	0.934	0.913
12H-3, 124	103.94	1.059	1.047	1.063	1.067
12H-5, 60	105.93	0.946	1.004	0.911	0.923
13H-3, 53	112.73	0.991	1.009	0.994	0.971
14H-2, 75	120.95	1.002	0.996	1.010	1.000
15H-3, 80	126.05	0.995	0.992	1.004	0.989
16H-3, 75	133.55	1.056	1.060	1.058	1.049

Table T13. Shear strength values, Hole 1246B.

Core, section, interval (cm)	Depth (mbsf)	Torvane (kPa)	Torvane size	ASV (kPa)
204-1246B-				
1H-1, 27	0.27			37.0
1H-1, 37	0.37	32.0	M	
1H-1, 57	0.57			28.5
1H-1, 58	0.58	33.0	M	
1H-1, 121	1.21			36.0
1H-1, 127	1.27	37.0	M	
1H-2, 35	1.85	39.0	M	
1H-2, 96	2.46	21.0	M	
1H-3, 22	3.22	41.0	M	
1H-3, 80	3.80	55.0	M	
2H-2, 103	5.73			47.0
2H-1, 125	5.95			55.0
2H-1, 132	4.99	38.0	M	
2H-1, 132	6.02	48.0	M	
2H-2, 82	7.02	51.0	M	
2H-3, 92	8.62	61.0	M	
2H-4, 90	10.10	64.0	M	
2H-5, 142	12.12	70.0	M	
2H-6, 20	12.40	75.0	S	
3H-1, 55	14.75	50.0	S	
3H-1, 89	15.09	60.0	S	
3H-2, 63	16.33	60.0	S	
3H-2, 113	16.83	72.5	S	
3H-3, 82	18.02	72.5	S	
3H-4, 103	19.73	62.5	S	
3H-4, 48	19.18	90.0	S	
3H-5, 86	21.06	80.0	S	
3H-6, 31	22.01	82.5	S	
4H-1, 135	25.05	55.0	S	
4H-2, 82	26.02	62.5	S	
4H-3, 67	27.32	75.0	S	
4H-4, 109	29.29	50.0	S	
4H-5, 80	30.50	95.0	S	
4H-6, 131	32.52	60.0	S	
5H-1, 37	33.57	67.5	S	
5H-2, 7	34.77	67.5	S	
5H-3, 106	37.26	65.0	S	
5H-4, 118	38.88	65.0	S	
5H-5, 25	39.45	90.0	S	
5H-6, 44	41.14	70.0	S	
6H-1, 133	44.03	90.0	S	
6H-2, 58	44.75	90.0	S	
6H-4, 120	48.30	90.0	S	
6H-5, 85	49.45	92.5	S	
6H-6, 106	51.16	105.0	S	
7H-2, 85	54.44	112.5	S	
7H-4, 90	57.44	75.0	S	
7H-5, 30	58.34	87.5	S	
7H-7, 48	61.07	87.5	S	
8H-2, 122	64.42	112.5	S	
8H-5, 108	68.78	130.0	S	
9H-1, 100	72.20	100.0	S	
9H-5, 53	77.44	100.0	S	
10H-1, 66	81.36	95.0	S	
10H-4, 73	85.93	120.0	S	
11H-2, 133	93.03	127.5	S	
11H-3, 82	94.02	115.0	S	
12H-1, 133	101.03	90.0	S	
12H-6, 142	108.25	120.0	S	
13H-1, 141	110.61	105.0	S	
13H-2, 65	111.35	105.0	S	
13H-2, 103	111.73	125.0	S	
13H-3, 55	112.75	87.5	S	
13H-3, 113	113.35	127.5	S	
13H-4, 35	114.05	105.0	S	
13H-5, 123	116.43	105.0	S	
13H-6, 47	117.17	100.0	S	
13H-6, 80	117.50	115.0	S	
14H-1, 43	119.13	137.5	S	
14H-2, 71	120.91	150.0	S	
15H-1, 117	123.57	137.5	S	
15H-2, 56	124.31	127.5	S	
15H-3, 48	125.73	147.5	S	
15H-4, 131	128.06	122.5	S	
15H-5, 84	129.09	122.5	S	
16H-1, 130	131.10	112.5	S	
16H-2, 97	132.27	120.5	S	
16H-3, 43	133.23	145.0	S	
16H-4, 65	134.95	127.5	S	
16H-5, 7	135.87	127.5	S	
16H-5, 25	136.05	105.0	S	

Notes: ASV = automated shear vane. M = medium, S = small.

Table T14. Temperature measurements, Hole 1246B.

Core	Depth (mbsf)	Temperature (°C)	Thermal conductivity (W/[m-K])	Tool ID
204-1246B-				
3H	23.7	5.72	0.93	12
5H	42.7	4.61	0.95	12
7H	61.7	6.27	0.96	12
9H	80.7	6.92	0.92	12
12H	109.2	7.95	0.95	12

Notes: No DVTP or DVTPP measurements were made at Site 1246.
ID = identification.